Short-Length Raptor Codes for Free-Space Optical Communications

SHORT-LENGTH RAPTOR CODES FOR FREE-SPACE OPTICAL COMMUNICATIONS

BY

WENZHE ZHANG, B.Sc.

A THESIS

SUBMITTED TO THE DEPARTMENT OF ELECTRICAL & COMPUTER ENGINEERING

AND THE SCHOOL OF GRADUATE STUDIES

OF MCMASTER UNIVERSITY

IN PARTIAL FULFILMENT OF THE REQUIREMENTS

FOR THE DEGREE OF

MASTER OF APPLIED SCIENCE

Master of Applied Science (2009) McMaster University
(Electrical & Computer Engineering) Hamilton, Ontario, Canada

TITLE:	Short-Length Raptor Codes for Free-Space Optical Communications
AUTHOR:	Wenzhe Zhang B.Sc., (Electrical Engineering) Peking University, Beijing, China
SUPERVISOR:	Dr. Steve Hranilovic
NUMBER OF PAGES:	xiii, 99

To my parents who supported my academic dreams from high school to univeristy

Abstract

Free-space optical (FSO) links are competitive wireless links offering high data rate, security and low system complexity. Compared to radio-frequency (RF) links, FSO links offer high rates at gigabit-per-second (Gbps) level and relatively low cost. However, atmospheric scintillation and misalignment between optical transmitter and receiver impair data rates of FSO links. Scintillation and misalignment are slow fading processes with a fading interval of 10's ms. Conventional fixed-length channel coding which interleave data blocks are unrealistic to overcome this slow fading due to block length of 10's of megabits. Also, because of the Gbps data rate, data rate adaptation to channel conditions are expensive.

In this work, short-length ($16 - 1024$) Raptor codes are designed to overcome the slow fading of FSO channels. These Raptor codes are applied at the packet-level with high data rate and low decoding complexity. The Raptor encoder and decoder can be easily implemented in any software or hardware form. The practicality of these Raptor codes is demonstrated by a Raptor encoder and decoder which are implemented in field-programmable gate array (FPGA) and shown to support a 1.22 Gbps encoding and 714 Mbps decoding rate with a 97 mW low power consumption and 26360 gate circuit scale. High-speed transmission at Gbps level is easily satisfied by the same design implemented in an application-specific integrated circuit (ASIC).

Two applications of these short-length Raptor codes in FSO links are presented in this work. Firstly, these Raptor codes are applied to hybrid FSO/RF links to achieve high data rate by sending Raptor encoded packets simultaneously over the FSO and RF links which we term such links as Raptor-coded soft-switching hybrid FSO/RF links. The performance of these Raptor codes in the hybrid FSO/RF links is simulated in a realistic channel model based on climate data of three Canadian cities. For a 1 Gbps FSO link combined with a 96 Mbps WiMAX RF link, the soft-switching system achieves an average rate of 472 Mbps using the implemented Raptor code while hard-switching technique achieves only 112 Mbps on average.

Secondly, these Raptor codes are applied in mobile FSO links for an unmanned aerial vehicle (UAV). This mobile FSO link suffers from severe instantaneous misalignment. For packet-level transmission, the time varying misalignment is unknown to the transmitter and causes data packet corruption and erasure. As a result, the application of conventional fixed-rate erasure coding techniques is difficult. In this work, short-length Raptor codes are applied in such mobile FSO channels. A key advantage of Raptor codes is their independence on channel state, no matter how large the misalignment. With a 1 Gbps transmitter, the designed Raptor code with $k = 64$ message packets offers 650 Mbps data rate when transmitting power is 20 dBm. In contrast, a traditional automatic repeat-request (ARQ) algorithm technique on the same FSO jitter channel achieves a rate of 70 Mbps.

Acknowledgements

In my great appreciation, I benefited a lot from my supervisor Dr. Steve Hranilovic during my two-year study and research in Electrical and Computer Engineering at McMaster University. From beginning to the end, from creating ideas to detail revisions, Dr. Hranilovic offers his full enthusiasm and patience to me. Every time when I am barricaded by troubles, he always encourages me to think deep and work hard to move on. I would also like to thank Cheryl Gies who does an excellent job in arranging the study and funding issues.

I also wish to thank Mr. Ahmed Farid, Mr. Mohamed D.A. Mohamed and Mr. Awad Dabbo who are senior members in my research group. Their kindness lets me feel free to study and work and their diligence impresses me. Warm discussions among us make me understand more than studying along.

My parents keep supporting my study from China to Canada. I can image how they miss me and contribute their love to me, the only child in the family. Though separated away thousands of kilometers, I have the same feeling of theirs. Sincere thanks to my parents for their love.

Contents

List of Figures

Chapter 1

Introduction

1.1 Motivation

Free-space optical (FSO) links provide line-of-sight (LOS) data links by modulating the instantaneous intensity of a laser and allowing it to propagate through the atmosphere to a receiver. Unlike radio-frequency (RF) links, FSO links do not require a spectrum license. FSO links offer communication security due to the point-to-point laser signal transmission avoiding interception. Data rates comparable to optical fiber transmission can be carried by FSO links with low system cost with a simple optical transmitter/receiver architecture. From the invention of laser in 1960's, the data rates of FSO links have increased steadily [1, 2]. Compared to the 100's Mbps maximum data rate of RF links, commercial FSO systems at data rate of 10 Mbps to 2 Gbps over a communication distance of $1 - 3$ km are available, and a data rate of 80 Gbps in lab has also been demonstrated [3–7]. However, the data rates of FSO links are limited by atmospheric scintillation and misalignment.

An important application of FSO links is to provide "last mile" access of high-speed internet connections in an urban optical wireless network [8], as shown in Fig. 1.1. In this network, the main building connected to backbone cable shares access with neighbour buildings through FSO links. Compared to a conventional wired network, this application of FSO links offers greater flexibility and lower cost. An example in Istanbul Turkey shows that an urban FSO network connecting nodes $1.2 - 2.3$ km apart offering 155 Mbps high-speed access to customers only costs \$1.4 million compared to the \$78.5 million cost of laying optical fiber [9]. A market study report in 2007 predicts that the consumption of point-to-point FSO systems will grow from \$13.68 million to \$15.77 million in North America, and from \$50.55 million to \$58.89 million in the global market in the period of 2009-2011 [10].

FSO links are also considered for mobile wireless links. FSO links with high data rates up to 1 Gbps are applied for civil and military uses connecting different mobile platforms such as unmanned aerial vehicle (UAV), high altitude platform (HAP) and satellite [11–16]. A UAV is a high-speed unmanned aircraft controlled by remote control from ground automatically. A UAV can patrol a given path at high speeds to collect battlefield information. Many UAVs with different size, range, height and payload specifications are employed fro military application [17, 18]. One possible military use is for soldiers to report battlefield information to a command post through a UAV. FSO links between soldiers and UAVs offer high data rate at Gbps sufficient to support video data and high security avoiding eavesdropping. The configuration of this application is shown in Fig. 1.2. An advantage of such links is the inherent security, however, misalignment must be overcome.

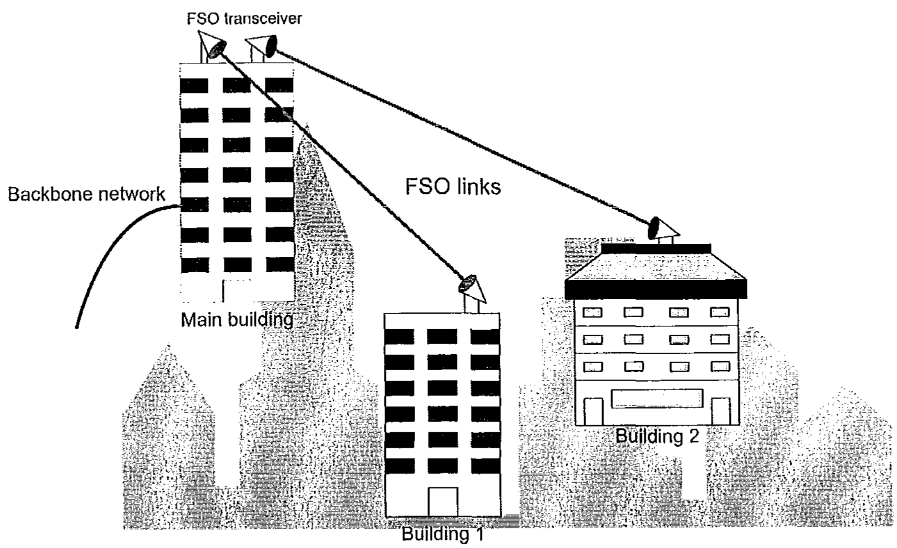

Figure 1.1: An urban FSO network between buildings

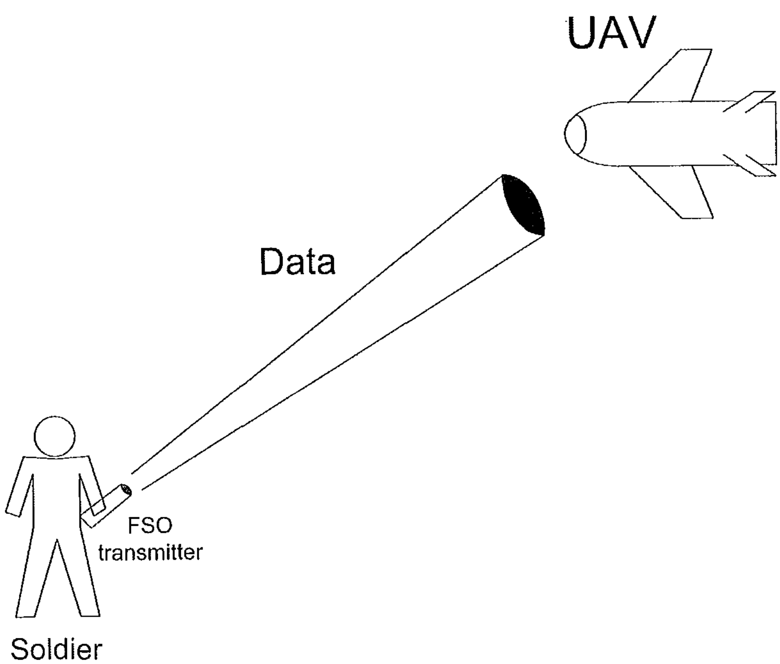

Figure 1.2: A military FSO ground-to-UAV link

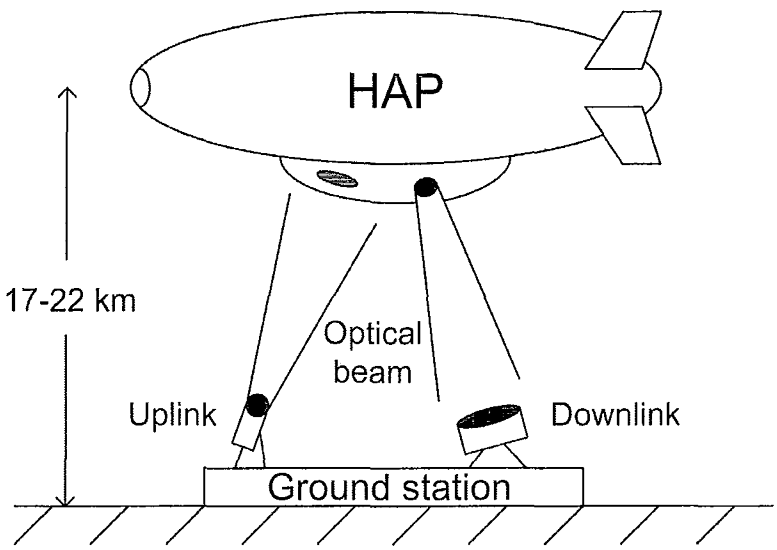

Figure 1.3: FSO links between a HAP and a ground station

A high-altitude platform (HAP) is a quasi-stationary aircraft floating in stratosphere altitude (17 – 22 km). Unlike regular aeroplanes, due to the huge floating volume filled with lighter-than-air gas, HAPs move in a higher altitude with a lower speed. Due to their high altitude, HAPs offer larger communication coverage compared to aeroplanes [19, 20]. Also, HAPs do not require expensive launching cost compared to satellite. For wireless communication purpose, HAPs with different size, shape and endurance are available [19–22]. A configuration of uplink and downlink FSO links between HAPs and ground stations is presented in Fig. 1.3. A key advantage of these mobile FSO applications is the Gbps data rate compared to 100's Mbps of RF links. Also, compared to the weight of 100's kg of RF terminals on mobile wireless platforms, the weight of FSO links is much less at 10's kg due to their simple architecture [23, 24]. An FSO link operating at 622 Mbps for a 64 km communication distance has been demonstrated with a light 17.54 kg terminal on the HAP [11].

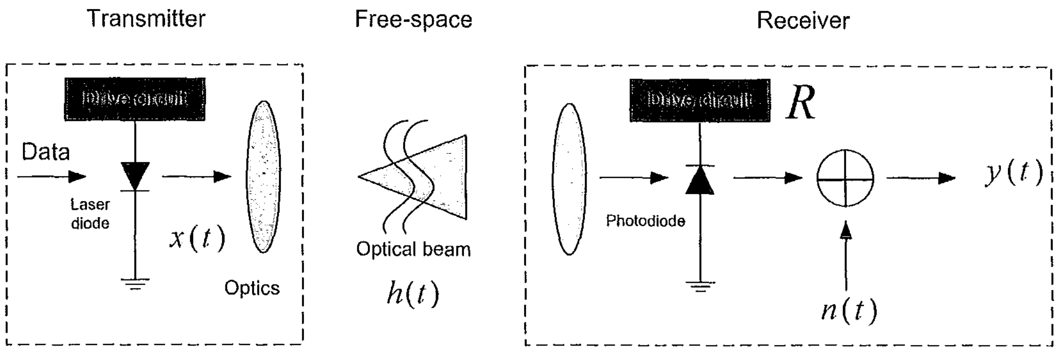

Figure 1.4: Diagram of FSO communications channel model

1.2 FSO Channel Model

Figure 1.4 presents a diagram of an FSO link with intensity modulation and direct detection (IM/DD). Transmitted and received FSO signals are optical intensity signals. In the FSO transmitters, data are modulated and output to laser diodes as current signals. Laser diodes convert electrical current signals into optical intensity signals which are non-negative. At FSO receivers, photodiodes convert the received intensity to an electrical current signal linearly. The drive circuit of photodiodes may contain amplifiers which amplify the tiny received signal significantly.

In order to minimize the geometric loss, the laser beamwidth of FSO links are generally designed with a small divergence angle of several mrad. High pointing alignment is required and optical signal propagates directly from transmitter to receiver requiring a line-of-sight. Multipath effects are neglectable in FSO links. Define continuous transmitted optical signal as $x(t)$ and received current signal converted by photodiode as $y(t)$. Also define channel impulse response as $h(t)$, receiver responsivity which is the ratio that converted current signal over received optical intensity at receiver as R and noise as $n(t)$. The continuous channel model of FSO links is modeled as,

$$y(t) = R \cdot x(t) \otimes h(t) + n(t), \tag{1.1}$$

where $\otimes$ denotes convolution. An automatic gain control circuit(AGC) is used to ensure an appropriate level of integrated $y(t)$ for bit-wise hard detection in commercial FSO links. Recent high-power laser diodes for FSO links offer an output range from 10's to 100's mW [3–5]. The wavelength of laser diodes is conventionally selected from $650 - 1550$ nm. Compared to radio-frequency (RF) links, a main advantage of FSO links is that the carrier frequency and bandwidth are license-free [25]. Slow fading $h(t)$ due to atmospheric scintillation and misalignment changes much slower at 10's of ms compared to the transmission bit interval at ns. Since the channel model of FSO links is memoryless and the delay of $h(t)$ is neglectable, $h(t)$ can be modelled as,

$$h(t) = h \cdot \delta(t), \tag{1.2}$$

where h is a constant gain in a coherence time and $\delta(t)$ is an impulse function. With (1.2), the convolution in (1.1) can be simplified to a multiplication of the instaneous $x(t)$ and h. The thermal noise of amplifier and shot noise generated by optical signal and ambient light are two major sources of $n(t)$. For point-to-point FSO links with a wide field-of-view (FOV) at receiver, the collected ambient light power is far greater than the optical signal and it is the dominant source of noise. Ambient light generally refers to natural light and $n(t)$ is modeled as additive, white and Gaussian noise [26–28].

The most common modulation technique for FSO links is on-off keying (OOK) with a direct detection. For an OOK transmitted bit interval T_b, assume that received current signal $y(t)$ is integrated to y, then (1.1) is modified to a discrete form as

$$y = hRx + n, \tag{1.3}$$

where x is the transmitted optical intensity, n is the noise and h is a discrete channel gain of the bit interval T_b [29]. For OOK, transmitted signal $x \in \{0, 2P\}$ equally likely and P is the average transmitted power. Unlike RF links, the transmitted signal of FSO links is always non-negative.

Generally, the channel gain h can be factored as,

$$h = h_l h_a h_g h_m, \tag{1.4}$$

where h_l is the atmospheric loss due to attenuation, h_a is the loss due to atmospheric scintillation, and h_g and h_m are the loss due to geometric loss of the divergence of optical beam and misalignment respectively. Atmospheric loss, h_l, is an attenuation caused by the scattering and absorption of the optical signal which is a constant loss effect for a given weather condition. Geometric loss, h_g, is an effect of the beam divergence. As presented in Fig. 1.5, the divergence of an optical beam can be represented by a divergence angle ϕ where the optical magnitude is only e^{-2} of the maximum magnitude in the centre of a Gaussian beam [30]. For a communication distance L, the effective beamwidth is defined as $w = L \cdot \phi$. To minimize h_g, narrow divergence beams are chosen.

Scintillation and misalignment are two sources of the fading of h. Due to their short wavelength, optical signal propagating in atmosphere is affected by atmospheric scintillation. Different air temperature and pressure in atmosphere causes variation

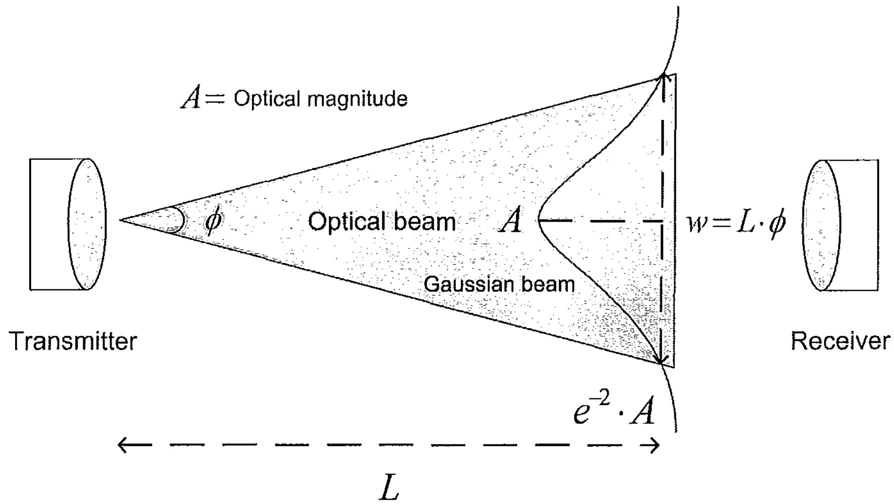

Figure 1.5: Geometric loss

of refractive index during the long-distance transmission of optical signal [29]. This variation causes fluctuation of the received optical intensity at receiver and it is modeled as a slow fading of h_a. This effect is called scintillation and it depends on the weather condition, such as clear or foggy. In the discrete channel model (1.3), h_a is randomly selected in every coherence time $T_f = 1 - 100$ ms from experimental result [31]. Compared to the Gbps transmission rate, the fading of scintillation is a very slow fading. An illustration of air turbulence is presented in Fig. 1.6 (a), where the pockets in the optical beam are the areas with different temperature or pressure [29]. An experimental result of atmospheric scintillation is reflected by the varying channel gain $h(t)$ in Fig. 1.6 (b), where the FSO link operates at 2.7 km communication distance and repeated pulses are transmitted at 2 MHz [31].

Another fading of h_m is caused by the misalignment between transmitter and receiver, as shown in Fig. 1.7. Since FSO links are designed with a small beamwidth with a several mrad divergence angle, a small sway of the transmitter or receiver

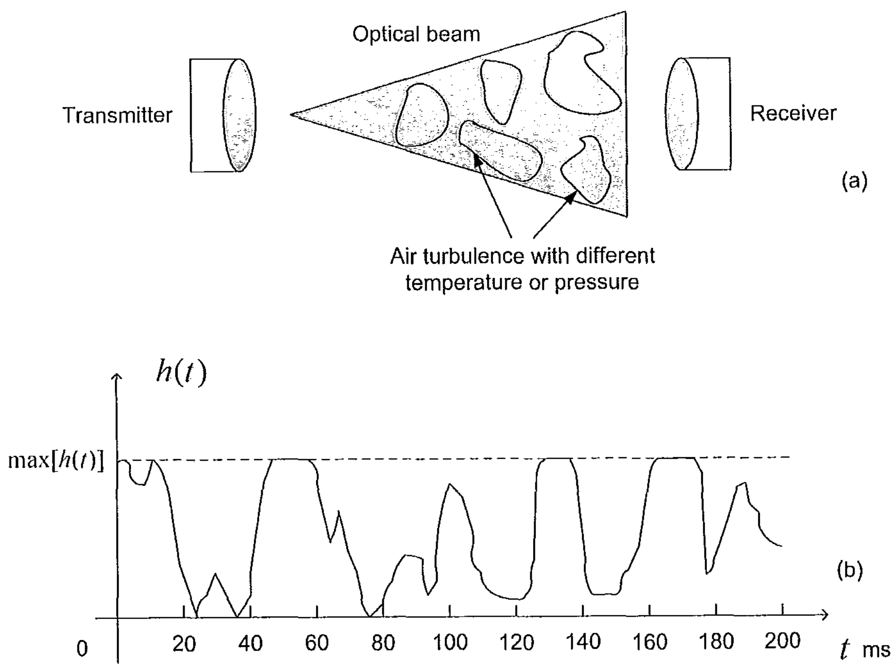

Figure 1.6: An example of atmospheric scintillation [29, 31]: (a) Scintillation area in an optical beam, (b) Time-varying $h(t)$ by caused scintillation

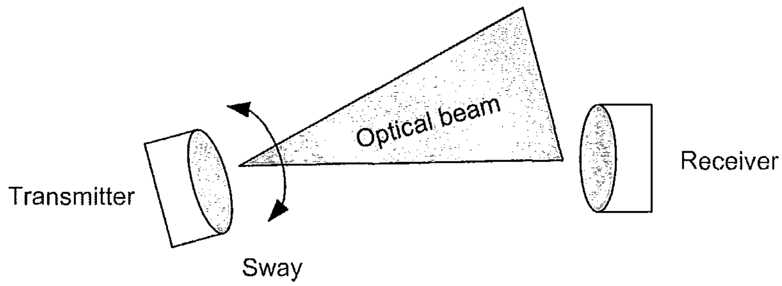

Figure 1.7: Fading due to misalignment

can cause significant fading. For fixed point-to-point applications such as urban FSO links, misalignment is caused predominantly by the sway of the buildings. The amplitude of sway of building ranges from 1/200 to 1/800 of the height of the building [32]. On the other hand, for FSO links applied in mobile platforms, motion between platforms is the major source of misalignment. The intensity of misalignment depends both on the motion of the FSO terminals and the optical beamwidth, ϕ, as shown in Fig. 1.7. A wide optical beam causes a big geometric loss of the received signal, but it may mitigate the fading of misalignment. The channel capacity of FSO links is limited by atmospheric scintillation and misalignment. The combination of atmospheric scintillation and misalignment has been studied in [30, 33, 34]. Details of scintillation and tracking error for different FSO channel models are presented in Chap. 3 and Chap. 4.

A direct thought to overcome these disadvantages of FSO links is to apply channel coding. Since scintillation and misalignment can both be modeled as random slow fadings, conventional fixed-rate channel codes with interleaving are too complex to overcome. For example, with a data rate of 1 Gbps and a coherence time T_f of 10's ms, the length of data blocks has to be 10's megabits. Another possible method to overcome the fading with fixed-rate channel codes is to adapt data rate assuming that channel condition is estimated at receiver and fed back to transmitter. However, for data rates at Gbps, the complexity of feedback and adaptation of fixed-length channel coding schemes makes it impractical. So, in this thesis, the main idea to overcome the slow fading is to use Raptor codes to adapt to channel conditions automatically with little feedback.

1.3 Review of FSO applications

1.3.1 Rateless Codes for FSO channels

Rateless codes are a random linear codes considered to overcome channel fading in many cases [35–37]. For bit-wise Raptor codes, forward error correction is applied. Raptor codewords corrupted by fading and noise are corrected by Belief Propagation (BP) algorithm, similar as LDPC. For Raptor codes applied at the packet-level, a proportion of the Raptor packets are erased and the rest are used to recover the message. Different from fixed-rate channel coding schemes, rateless codings do not have a fixed number of transmitted encoded symbols, so it is called rateless. For a given k-symbol message, rateless encoder keeps generating encoded symbols until the decoder gets enough symbols to decode the message. The number of received symbols to decode depends on k and the channel condition. When the rateless decoding is finished, a terminate feedback signal is sent from decoder to encoder to stop the encoding process. Luby transform (LT) codes are the first kind of rateless codes and Raptor codes are improved from LT codes offering higher rate and lower decoding complexity. Due to the more flexible design of Raptor codes, they have better performance than LT codes [35, 38]. Previous work on Raptor codes have developed long-length Raptor codes $k = 9500 - 120000$ [35, 36]. Previous Raptor code implementations have been reported at several Gbps data rate on a 2.4 GHz Intel Xeon CPU, and 27 Mbps on a 206 MHz Intel StrongARM processor [35, 39].

The Raptor encoded packets are linear combinations of message packets. The connection information (CI) of degree and which message packets are connected of an encoded packet is necessary for decoding. Previous work on FSO channels with Raptor codes applies synchronized Raptor encoder and decoder [40]. The CI of Raptor packets is generated both by synchronous encoder and decoder. However, this synchronization is unrealistic because a small delay in the CI generation can cause significant error in decoding especially when a long communication distance exists.

1.3.2 Hybrid FSO/RF Links

The reliability of FSO links is limited by atmospheric conditions such as foggy. For fixed point-to-point links, hybrid free-space optical/radio-frequency (FSO/RF) links have been considered as a competitive solution for high-speed wireless communications [41, 42]. They combine the advantages of the two links by inheriting the high data rate of FSO links and the reliability of RF links. Products for different data rates from 10 Mbps to multiple Gbps are currently available [43]. Hybrid FSO/RF links have also been considered for mobile applications such as robot remote control in complex environments [44, 45].

Due to their very different carrier frequencies, FSO and RF channels have distinct channel impairments. The short wavelengths used in FSO links are severely affected by scattering due to fog and atmospheric scintillation while RF links are particularly sensitive to rain scatter. Using both links in a system to overcome these unique

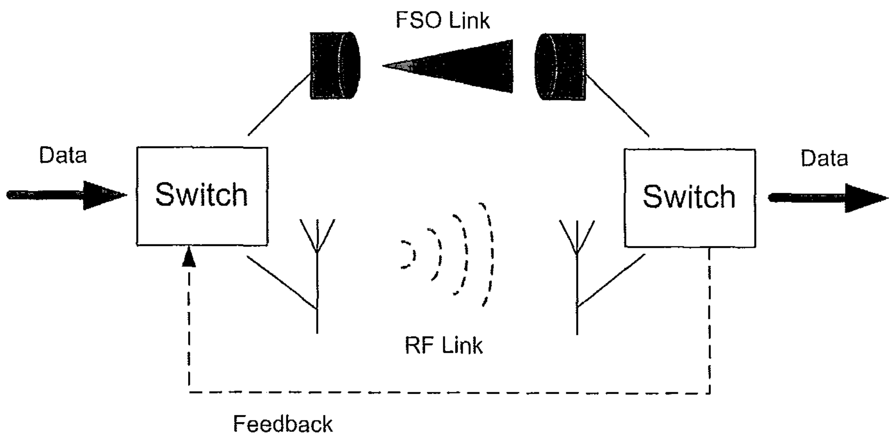

Figure 1.8: Diagram of hybrid FSO/RF links.

channel impairments can result in a gain in reliability or rate, however, is highly dependent on the configuration employed.

Figure 1.8 presents a configuration of a hybrid FSO/RF link. In a hard-switching scheme, the transmitter and receiver jointly select either the FSO or RF channel for data transmission. The high-data rate FSO link is selected only if channel conditions permit reliable communications, otherwise all data are sent over the RF channel [46]. Notice that the transmitter and receiver must be co-ordinated via feedback to select the correct channel for transmission. A key disadvantage of hard-switching is that at any time one link is sitting idle. In practice, scintillation or loss in the sensitive FSO channel will cause it to be selected rarely. Once the RF link is selected, the channel capacity of FSO link is wasted.

An idea to overcome the hard-switching disadvantage is to co-ordinate data transmission in both links using channel coding called soft-switching. In this soft-switching scheme, the switches in Fig. 1.8 are replaced by an encoder and decoder. In [47], data are encoded by a single LDPC code with a portion of the codeword split to FSO and RF links and the rate is adjusted via puncturing according to instantaneous channel conditions. Although this technique improves over hard-switching, channel conditions must be known at transmitter and receiver and complex soft decoding is required which is difficult at FSO data rates. Raptor codes have also been recently considered for hybrid FSO/RF links [35, 40]. These codes do not require channel knowledge at the transmitter and are able to adapt their rate to channel conditions. In [40], a bit-wise Raptor coding scheme is considered in which bits transmitted on FSO and RF links are random linear combinations of message bits. A well-known code is employed [35], and it is assumed that the transmitter and receiver have the interconnection information for each bit. Additionally, complex soft iterative detection is required at the receiver and the impact of varying atmospheric conditions is not considered.

1.3.3 Mobile FSO Links

Although most FSO links are stationary, they have also been considered for mobile applications. Applications such as ship-to-ship, ground-to-air and air-to-air FSO communication systems have been studied [12, 13, 48]. FSO links satisfy the needs of long-range deep-space communications [49] and have also been considered for military wireless communications [50].

A possible application of mobile FSO links is the ground-to-UAV link as presented in Fig. 1.9. To make alignment between the optical transmitter and receiver, mobile FSO links face the pointing, acquisition and tracking (PAT) problem because of the severe motion of UAVs. Pointing is a process that optical beam from ground is pointed to the position of UAV. Acquisition refers the capture of the position of

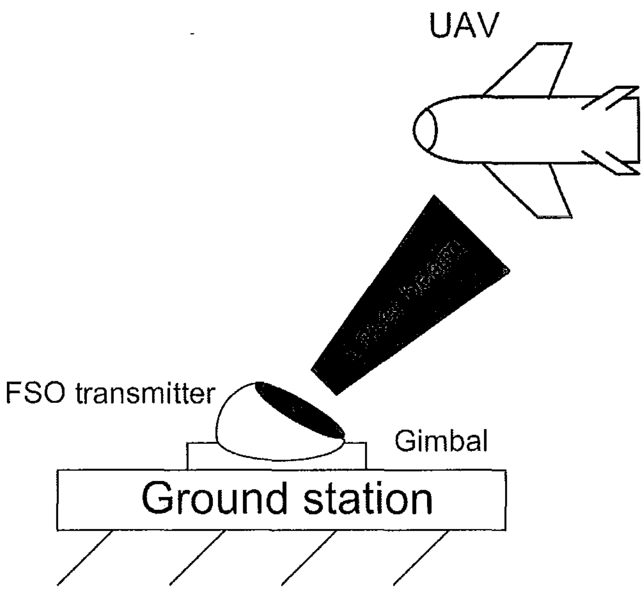

Figure 1.9: A ground-to-UAV FSO link

UAV from the initial uncertainty. Tracking means to keep the UAV covered by the optical beam after acquisition during the motion of UAV. In mobile FSO channels, the transmitter must track the motion of the receiver in order to maintain a LOS link. FSO transmitters on the ground can be hand-held or implemented on more stationary platforms such as vehicles with gimbals. Consider the FSO link in Fig. 1.9 where the speed of the UAV can reach several hundred meters per second [51]. In this scenario, tracking is typically accomplished by mechanical components such as a 2-dimensional rotating gimbal which is oriented based on fed back global positioning system (GPS) data from the UAV [12, 13]. Tracking is made more difficult due to the use of FSO transmitters with a small divergence angle to minimize geometric loss. A dramatic variation in the received SNR is caused by misalignment of the transmitted beam and the detector due to mechanical pointing uncertainty error and GPS positioning error. The total tracking error is the combination of these two errors and limits the data rates of such links.

For these severe jitter channels, the total tracking error is unknown to the transmitter and changes slowly in time with respect to the bit period. Link parameters and a tracking model with GPS of FSO links to UAV have been considered in [52–54]. In order to improve the data rates of such links, coding techniques can be considered. Fixed-rate coding techniques are not appropriate for such links due to the lack of channel state information and the slow variation of the channel.

1.4 Contributions of the Thesis

In this work, Raptor codes are applied to a variety of FSO channels. Received packets corrupted by fading and noise are detected by a cyclic redundancy check (CRC) code and dropped. The FSO channel is modeled as a packet erasure channel and the erasure correction performance of Raptor codes with 1-bit feedback per message is considered for hybrid FSO/RF and mobile channels.

Earlier Raptor code designs have lengths of at least 9500 [36] and are impractical for high rate at order of Gbps due to the excessive decoding cost. In this work, a novel set of short-length $(16-1024)$ Raptor codes are designed to achieve high rate and low decoding complexity. The design and statistical performance of these Raptor codes are presented in Chap. 2. The practicality of these Raptor codes is also demonstrated by a practical Raptor encoder and decoder which are implemented in an FPGA and shown to support a 1.22 Gbps encoding rate and 714 Mbps decoding rate with a low 97 mW power consumption and 26360 gate circuit scale in Chap. 2. The design and implementation of short-length Raptor codes have been presented in [55, 56].

Two applications of Raptor codes in hybrid FSO/RF links and mobile FSO links of UAVs are presented in Chap. 3 and Chap. 4 respectively. In Chap. 3, a practical soft-switching hybrid FSO/RF system is designed using short-length Raptor codes. Packet transmission is considered on FSO and RF channels due to its simplicity and wide spread use. The performance of the Raptor codes are simulated under the climate data of three Canadian cities. For a 1 Gbps FSO link combined with a 96 Mbps WiMAX RF link, the soft-switching system achieved an average rate of over 472 Mbps using the implemented Raptor code while hard-switching techniques achieved only 112 Mbps on average. This application has been presented in [55].

In Chap. 4, to overcome the severe jitter, short-length Raptor codes are applied in a mobile ground-to-UAV FSO link. Using the short-length Raptor codes defined in Chap. 2, detailed numerical simulations of the designed system are presented. In simulation, both scintillation and tracking error are considered. A key advantage of Raptor codes is their independence on channel state, no matter how large the misalignment. With a 1 Gbps transmitter, the designed Raptor code with $k = 64$ message packets offers 650 Mbps data rate when transmitting power is 20 dBm. In contrast, a traditional automatic repeat-request (ARQ) algorithm technique on the same FSO jitter channel achieves a rate of 70 Mbps. This result has been presented in [56].

1.5 Thesis Organization

This thesis is organized as follows: design and implementation of short-length Raptor codes are presented in Chap. 2. In Chap. 3 and Chap. 4, applications of short-length Raptor codes in hybrid FSO/RF links and in Mobile FSO links of UAVs are presented respectively. The thesis is concluded in Chap. 5 with directions of future work.

Chapter 2

Design and Implementation of Short-Length Raptor Codes

In this chapter, for many hybrid and mobile applications introduced in Chap. 1, the FSO channel is modeled as erasure channel and a set of short-length Raptor codes are designed and implemented to overcome the slow fading. The background of Raptor codes is presented in Sec. 2.1 and the erasure correcting performance is defined in Sec. 2.2. In Sec. 2.3, the design of Raptor codes is presented by details. As described in Chap. 1, previous work on Raptor codes with feedback requires the encoder and decoder operate in a synchronous way i.e., it is assumed that transmitter and receiver have synchronized random generators [40]. However, this synchronization is fragile when a long communication distance exists and a little delay can cause significant error in decoding. In this work, asynchronous hardware Raptor encoder and decoder in which interconnection information is added in each packet are designed and implemented in Sec. 2.4.

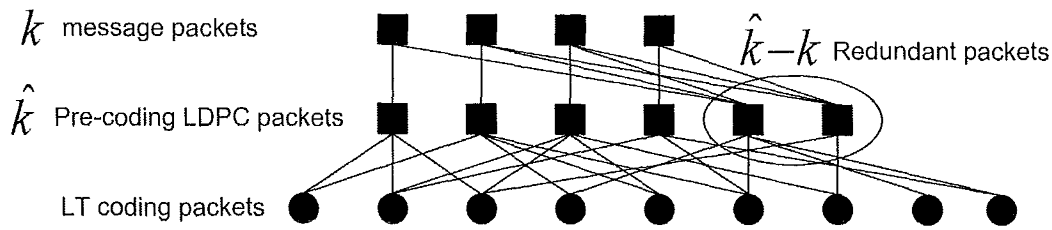

Figure 2.1: Factor graph of a Raptor code.

2.1 Background on Raptor Codes

Raptor codes are closely related to Luby transform (LT) codes [38] and are random bipartite graph codes in which every encoded packet is a linear combination of a random number of message packets. The *degree* of an encoded packet is the number of message packets combined, and is chosen randomly and independently for each encoded packet. Raptor codes have an outer low-density parity-check (LDPC) pre-code for the message packets. This LDPC pre-code enlarges the effective number of message packets from k to $\hat{k}$, as shown in Fig. 2.1. The *degree distribution* polynomial of a Raptor code is defined as $\Omega(x) = \Sigma_{i=1}^{\hat{k}} \Omega_i x^i$, where the x^i term represents a degree i, and Ω_i is the probability mass of degree i. Both LT and Raptor codes are decoded via a simplified belief propagation (BP) algorithm. The algorithm starts from a degree one packet and uses it to decode packets of larger degree. Decoded packets are subtracted from all larger degree packets which involve it. All received packets are stored in a buffer and the decoding process continues searching and subtracting until the k message packets are recovered. Section 2.4 presents efficient hardware implementation of a Raptor encoder and decoder.

The decoding complexity of a Raptor code has been shown to be $O(k \log 1/\eta)$ on average, where $\eta > 0$ is a design code overhead set typically at a couple percent [35].

Selecting a short k is advantageous to reduce complexity in decoding. However, in earlier Raptor code designs [35], an apparent trend is that reducing k resulted in a reduction in average rate. A $k = 9500$ Raptor code has also been widely used [36], however, for the Gbps rates considered for FSO channels, decoding such a code is complex.

The first Raptor code with $k \geq 64536$ in [35] is used for erasure correction. The problem of Raptor codes in [35] is that the long length limit their practicality especially for high-speed communications such as FSO links. A set of systematic fixed-length Raptor codes of length $k = 4 - 8192$ has been developed for forward error correction applications [37]. However, Raptor codes in [37] are applied without feedback, i.e., without adaptation to channel conditions. Moreover, the codes in [37] have a limited correction capability due to their fixed length which is similar as LDPC but different from general rateless codes. The error probability after correction of the fixed-length codes varies depending on channel conditions. In this case, a set of short-length $k = 16 - 1024$ Raptor codes which adapt to channel conditions using limited feedback is designed. A direct thought to apply Raptor codes with a little feedback is to apply them at packet-level and model the channel as packet erasure channel. This idea has been applied in a multimedia broadcasting network as shown in Fig. 2.2. For the network application, Raptor packets are sent through multiple channels from transmitter to receiver to utilize all the capacities of channels without knowing the channel state information. The receiver collects the Raptor packets until a sufficient number is received to finish decoding and sends a feedback signal to transmitter to stop the transmission [57–59].

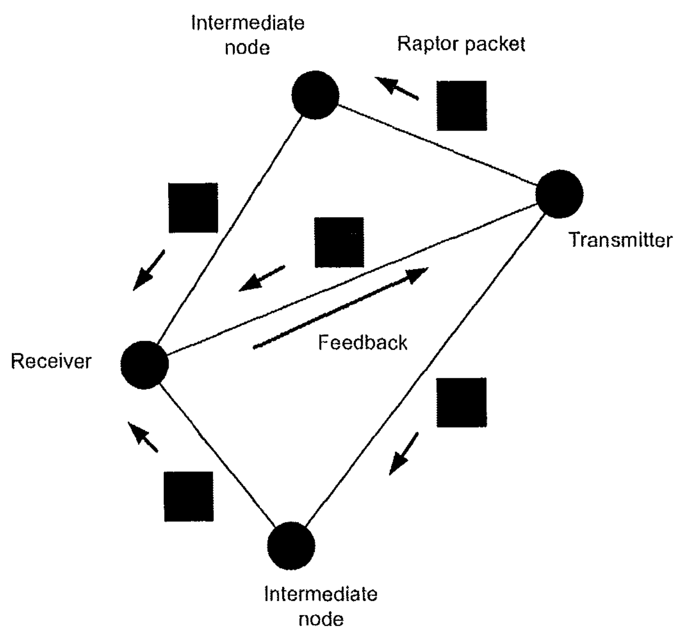

Figure 2.2: Illustration of multimedia broadcasting network with Raptor codes

2.2 Erasure Correcting Performance of Raptor Codes

Different from fixed-length codes, the rate of Raptor codes is in fact random. The number of packets needed for decoding depends on not only Raptor code itself, but also packet erasure probability θ $(0 \leq \theta < 1)$. In FSO channels, θ can vary in different weather conditions. To investigate the performance of Raptor codes in a packet erasure channel, in this section, the erasure correcting performance of Raptor codes is defined first.

Definition 1: For an erasure channel with erasure probability θ, a k-packet message is given. Define n, m as the number of transmitted and received packets required for successful decoding respectively.

Definition 2: Under sufficient observation of the decoding process, define $\Pr(n)$, $\Pr(m)$ as the probability of the event that instaneous n packets are transmitted, m

packets are received for successful decoding respectively. Also, define $\Pr(n|m)$ as the probability that n packets are transmitted when m packets are received.

The statistics m and $\Pr(m)$ can be obtained by simulation [60]. Define $\langle m \rangle$ as the expectation of m and

$$\langle m \rangle = (1 + \varepsilon_m)k, \tag{2.1}$$

where ε_m is the overhead of a k-length Raptor code. Though the rate of a Raptor code is random, $\langle m \rangle$ is a statistical measurement analogous to the code rate of fixed-length codes. The erasure correcting performance of a $k = 64536$ Raptor code in [35] is represented by the $\Pr(m)$ and $\langle m \rangle$ in Fig. 2.3 with a degree distribution as,

$$\begin{aligned}\Omega^*(x) &= 0.007969x + 0.49357x^2 + 0.16622x^3 + 0.072646x^4 \\ &+ 0.082558x^5 + 0.056058x^8 + 0.037229x^9 + 0.05559x^{19} \\ &+ 0.025023x^{65} + 0.003135x^{66}.\end{aligned} \tag{2.2}$$

To investigate $\Pr(n)$ in a specific erasure channel with θ, it is assumed that $\Pr(m)$ of a Raptor code is known. Since $n \geq m$, $\Pr(n)$ is expanded with $\Pr(n|m)$ and $\Pr(m)$ as,

$$\Pr(n) = \sum_{m=1}^{n} \Pr(n|m) \cdot \Pr(m) \tag{2.3}$$

The meaning of $\Pr(n = N|m = M)$ where N and M are instaneous values of n and m can be described in this way: For M received packets required for decoding, consider the specific case that the message is not recovered after $N-1$ packets are transmitted. In this case, for the $N-1$ transmitted packets, only $M-1$ packets are received. And the last transmitted packet, if it is received, the number of total received packets

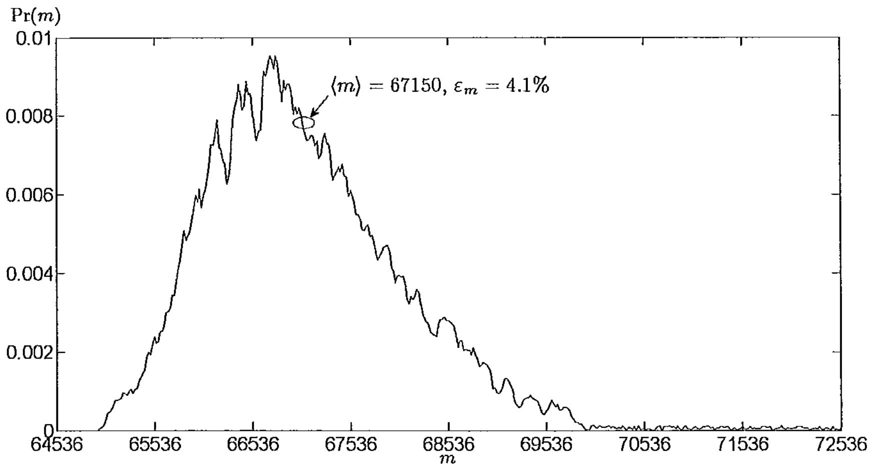

Figure 2.3: Probability of mass function, $\Pr(m)$, for number of received packet required for decoding $k = 64536$ in [35]

increases to M and decoding completes. $\Pr(n = N|m = M)$ is defined as,

$$\begin{aligned}\Pr(n = N|m = M) &= \overbrace{\binom{N-1}{M-1}\theta^{[(N-1)-(M-1)]}(1-\theta)^{M-1}}^{N-1 \text{ transmitted packets}} \cdot \underbrace{(1-\theta)}_{\text{last transmitted packet}} \\ &= \binom{N-1}{M-1}\theta^{N-M}(1-\theta)^{M} \qquad (2.4)\end{aligned}$$

where $\binom{N-1}{M-1}$ is the number of $M-1$ combinations from $N-1$. Substitute in (2.4) to (2.3),

$$\Pr(n) = \sum_{m=1}^{n} \binom{n-1}{m-1}\theta^{n-m}(1-\theta)^{m}\Pr(m) \qquad (2.5)$$

From (2.5), $\langle n \rangle$ is expressed as,

$$
\begin{aligned}
\langle n \rangle &= \sum_{n=1}^{\infty} n \cdot \Pr(n) \\
&= \sum_{n=1}^{\infty} n \cdot \sum_{m=1}^{n} \binom{n-1}{m-1} \theta^{n-m} (1-\theta)^m \Pr(m) \\
&= \sum_{m=1}^{\infty} \sum_{n=m}^{\infty} n \binom{n-1}{m-1} \theta^{n-m} (1-\theta)^m \Pr(m) \\
&= \sum_{m=1}^{\infty} (1-\theta)^m \Pr(m) \sum_{n=m}^{\infty} n \binom{n-1}{m-1} \theta^{n-m} \\
&= \sum_{m=1}^{\infty} (1-\theta)^m \Pr(m) \left[m(1-\theta)^{-m-1} \right] \\
&= \frac{\langle m \rangle}{1-\theta}. \qquad (2.6)
\end{aligned}
$$

As a statistic of n, $\langle n \rangle$ is just a multiple of $\langle m \rangle$ with the multiplier $1/(1-\theta)$, which depends on to the erasure channel. Therefore, a good Raptor code with small $\langle m \rangle$ still achieves small $\langle n \rangle$ for any arbitrary θ ($0 \leq \theta < 1$).

For FSO links modeled as erasure channels, the erasure probability θ is unknown at transmitter and receiver and varies significantly under different weather conditions. Conventional fixed-length codes are not suitable for this erasure channel because of the channel state is unknown and changes over time. Raptor codes and Luby transform (LT) codes [38] are called rateless codes where each packet is a random combination of message packets. Every Raptor or LT encoded packet is a random combination of message packets and the encoder keeps generating packets until the decoder collects sufficient number of the Raptor packets. No matter how big θ is, some of the Raptor packets are erased, but the remaining packets pass the channel. The specific packets received are not important, merely the number, θ only changes the rate of Raptor

Table 2.1: Degree of LDPC Pre-Code and c for different k

k	16	32	64	128	256	512	1024
D	9	16	19	27	30	33	44
c	0.04	0.05	0.05	0.07	0.08	0.08	0.09

codes which adapts to the channel capacity.

2.3 Design of Short-Length Raptor Codes

A key design parameter for any Raptor code is the average rate $\langle m \rangle / k$. Another key property of a Raptor code is the decoding complexity. Since every Raptor encoded packet is a linear combination of a couple of message packets. The number of message packets connected to an encoded packet is termed degree. Average degree, d_{avg} of a Raptor code represents the decoding complexity. In previous work [35], it is demonstrated that an increasing k causes a decreasing ε_m and an increasing d_{avg}.

2.3.1 Pre-Coding LDPC

In this work, for simplicity, the outer LDPC code is selected to be systematic and right-regular where each check node has degree D. The D message packets connected to each check node are chosen uniformly and independently. To each message, $\hat{k} - k = 0.02k$ redundant LDPC packets are added for $k = 64$ to 1024, and a single packet is added for $k = 16, 32$. Table 2.1 lists the selected degree D, of each redundant packet for different k. Initially, D was set to $\log_2 k$ and increased to minimize ε_m after simulation. Note, this heuristic optimization is typical in the design of such codes, and different pre-coding LDPC codes can achieve similar performance [35].

2.3.2 Design of Degree Distribution

The *input ripple* is defined as the set of message packets decoded up to a particular step [35]. A good code maximizes the input ripple throughout the decoding process. Reference [35] gives a heuristic proposal: for $x \in [0, 1-\delta]$, where δ is the fraction of message packets not decoded, keep the ripple size $\geq c\sqrt{(1-x)\hat{k}}$, where c is a small constant. Using this proposal, it was shown that $\Omega(x)$ should satisfy

$$\Omega^{'}(x) \geq \frac{-\ln(1 - x - c\sqrt{\frac{1-x}{\hat{k}}})}{1+\eta}, x \in [0, 1-\delta] \tag{2.7}$$

where $\Omega^{'}(x)$ is the derivative of $\Omega(x)$ [35].

In this work, for a given degree distribution in [35], (2.7) is verified by discretizing the interval $[0, 1-\delta]$ in steps of 0.001. Since there are many degree distributions satisfying (2.7), the design of $\Omega(x)$ for short k is based on the degree distribution for a long Raptor code of $k = 64536$ as $\Omega^{*}(x)$ described in (2.2) [35]. A heuristic technique must be applied to find $\Omega(x)$ for $k = 16$ to 1024 since no analytical design procedures exist. A typical value $\eta = 0.05$ is selected as in [35]. Following [35], to verify (2.7), $c < \delta\sqrt{\hat{k}}$ and $\delta = 0.01$. Care must be taken in selecting the value of c to ensure (2.7) is satisfied. Table 2.1 lists the values of c chosen after extensive simulation. To find an $\Omega(x)$ with good performance, $\Omega^{*}(x)$ is modified stepwise until (2.7) is satisfied.

Step 1: Truncate the large degree items in $\Omega^{*}(x)$ larger than $k/4$. For example, x^5 to x^{66} terms are removed for $k = 16$. From [35], it is not necessary that $\Omega(x)$ have packets of every degree. Figure 2.4 has an example of a truncated Raptor code with lower $\langle m \rangle$ than a comparable LT code which has all possible degree packets.

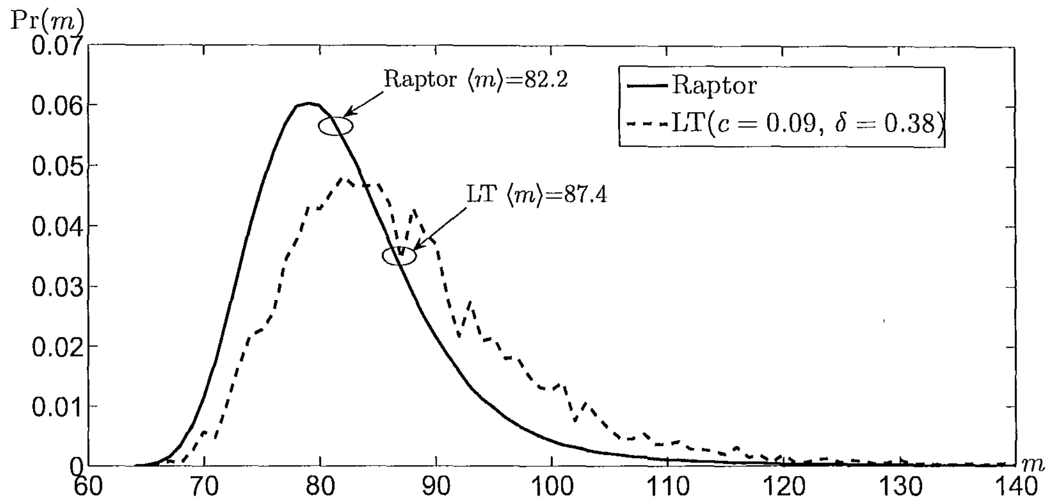

Figure 2.4: $\Pr(m)$ of Raptor code and LT code for $k = 64$

Qualitatively, adding large degree packets also increases d_{avg} significantly.

Step 2: Add x^{11}, x^{13}, x^{16} and x^{25} to $\Omega(x)$ for $k = 64$, 128 and 256. Packets of large degree are important to ensure that all message packets are covered. However, for the small k considered, the large degrees in $\Omega^*(x)$ are excessive. Therefore, moderate degree terms are added as a trade-off between x^9 and x^{66} terms.

Step 3: Increase probabilities Ω_i for small degrees significantly, especially for degree one. For example, for $k = 16$, increase Ω_1 from 0.007969 to 0.18. After $\Omega^*(x)$ is truncated in step 1, Ω_i of large degree terms is shifted to smaller degrees. If Ω_1 increases, more packets of degree one are sent in early stages of decoding. This shifting also reduces d_{avg}, the average decoding cost. Increasing Ω_1 too much, however, can stall decoding since the encoded packets may not cover enough message packets. Therefore, Ω_1 is increased and checked via simulation to ensure good operation.

After the heuristic steps above, an initial $\Omega(x)$ is obtained for each k. However, the initial design is often not robust and has large d_{avg} and ε_m. A simulation-based

Table 2.2: Design results for $\Omega(x)$

k	16	32	64	128	256	512	1024
Ω_1	0.18	0.11	0.1	0.06	0.04	0.025	0.015
Ω_2	0.52	0.5	0.5	0.495	0.495	0.495	0.495
Ω_3	0.1	0.13	0.11	0.16	0.167	0.167	0.167
Ω_4	0.2		0.08	0.08	0.08	0.082	0.082
Ω_5		0.26	0.042	0.05	0.07	0.071	0.071
Ω_8				0.037	0.039	0.05	0.049
Ω_9			0.045	0.02	0.025	0.044	0.048
Ω_{11}			0.06				
Ω_{13}			0.063				
Ω_{16}				0.04			
Ω_{19}				0.058	0.035	0.043	0.05
Ω_{25}					0.049		
Ω_{66}						0.023	0.023

technique is used to refine this initial $\Omega(x)$ to improve performance. For each k and choice of $\Omega(x)$ many simulations are performed to estimate the distribution of m. An example is shown in Fig. 2.4 for $k = 64$ for 10^8 iterations. Qualitatively, if ε_m is large from simulation, then more probability is shifted from large degree to small degree. This search procedure continues in this fashion until ε_m cannot be reduced any further. Table 2.2 presents the resulting degree distributions.

2.3.3 Results of Code Design

The performance of the codes define in Tbl. 2.2 is plotted in Fig. 2.5. Notice that ε_m decreases with increasing k. When $k = 1024$, ε_m decreases to 0.126. However, d_{avg} increases with k. For $k = 1024$, $d_{\text{avg}} = 6.32$, which can be considered as a moderate decoding cost. Compared to $k = 64536$ code using $\Omega^*(x)$ from (2.2) [35], coding overhead, ε_m, for $k = 1024$ is 8% larger than for $k = 64536$, however, d_{avg}

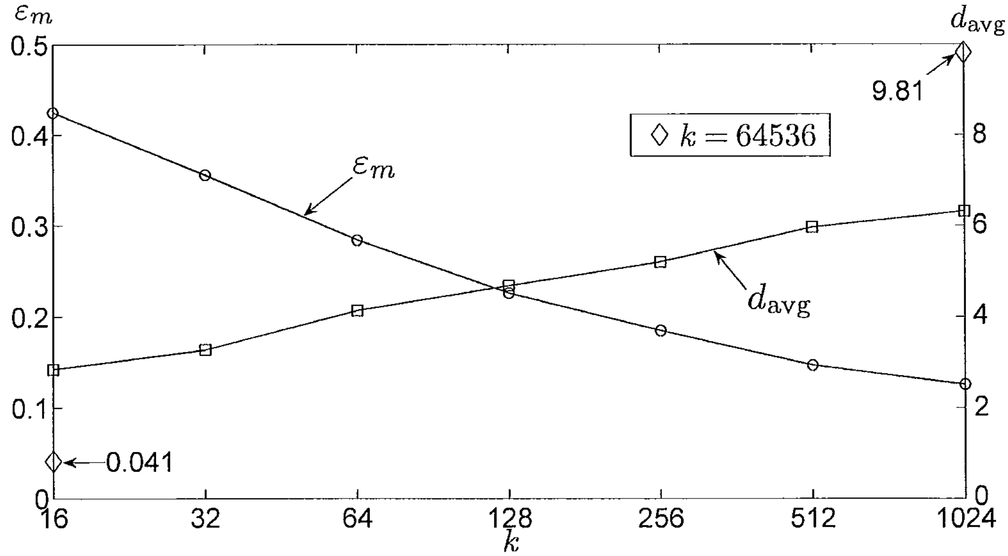

Figure 2.5: Overhead, ε_m, and average degree, d_{avg}, of Raptor codes

is approximately 37% less. The comparision between $k = 16$ and $k = 64536$ shows that d_{avg} of the smaller k is about a quarter of the bigger k. In Raptor decoding, this means $k = 16$ can be decoded fast at least as 4 times as that of $k = 64536$. For instance, a Raptor decoder which only works at 250 Mbps for $k = 64536$ can work at 1 Gbps for $k = 16$. This is a significant trade-off between a slight increase in coding overhead ε_m and a large decrease in decoding complexity, i.e., d_{avg}.

2.4 Implementation of Raptor Encoder and Decoder

Unlike the synchronous Raptor encoder and decoder presented in [40], in this chapter, asynchronous Raptor encoder and decoder without synchronization are applied. For the Raptor encoded packets, degree and connection to message packets are generated

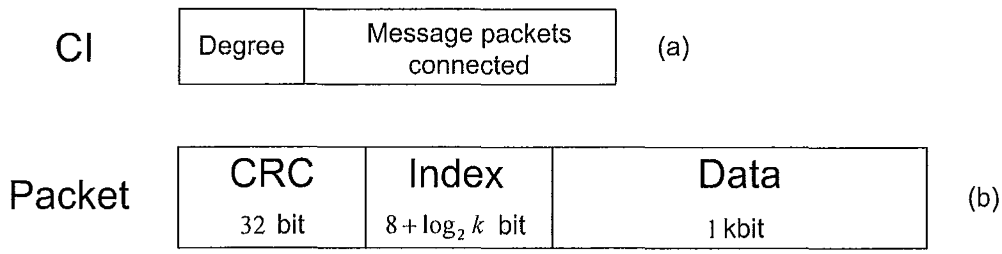

Figure 2.6: Connection information and packet structure

randomly. It is not practical to assume transmitter and receiver have synchronized random generators. Thus, every encoded packet must contain its interconnection information. In this work, define the *connection information*, (CI), of an encoded packet as its degree and the list of all message packets used to construct it, as shown in Fig. 2.6(a). Notice that the number of bits required to encode the CI for a particular packet can vary significantly. In order to obtain a fixed-size transmitted packet, a finite set of CI's are stored at both transmitter and receiver in a table termed the *CI table* (CIT). Thus, only the index into this table need to be transmitted with each packet. If an index is known, the corresponding CI is known, and decoding can proceed. Adding an index to packets causes extra redundancy, however, compared to a large data size, this extra redundancy is trivial. For $k = 16 - 1024$, the size of index is $8 + \log_2 k$ bit, less than 2% of the packet for $\ell = 1024$, as shown in Fig. 2.6(b). In Sec. 2.4.7 the size of the memory required for the CIT is quantified in a practical implementation.

In this section, the particular algorithms of Raptor encoding and decoding are presented first. These realistic algorithms can be implemented both in software and hardware easily. Secondly, architectures of the Raptor encoder and decoder are described in detail. Finally, implementation in an FPGA including experimental results of encoding/decoding speed, circuit scale and power consumption is presented.

2.4.1 Algorithm of Raptor Encoder

The encoder requires a mechanism to generate random degrees according to $\Omega(x)$ as well as an LDPC generator for pre-coding. After a degree is selected, a set of message packets equal to the degree are selected randomly and uniformly from the message packets. In this work, to simplify implementation, the random generator is replaced by the pre-computed CIT. This table is formed by using a pseudorandom generator to select degrees according to $\Omega(x)$. In addition, the interconnection of the LDPC pre-coded packets are included in the entries of the CIT. In order to ensure good performance, the length of the CIT must be long enough to thoroughly sample possible degree selections. In this work, after extensive simulation, the CIT table is set to contain $256 \cdot k$ elements. The same CIT is implemented at both encoder and decoder.

A variable *index* is defined which refers to an index in the CIT. For a given index the CI is known and the data of the indicated packets are combined through exclusive-or (XOR). Then the index is appended to the encoded data and a CRC is added. After the encoding of a packet is completed, the encoder moves to the next packet and the index in the CI is incremented. If current message is finished, the encoder moves to the next message.

2.4.2 Algorithm of Raptor Decoder

The Raptor decoder is far more complicated than the encoder. Define *undecoded packets* (UDP) as received packets whose degree is greater than 1. Conversely, define *decoded packets* (DP) as degree one packets which have been released in previous decoding stages. Finally, define *newly released packets* (NRP) as degree one packets which are released in the current decoding stage. Undecoded packets, decoded packets and newly released packets are stored separately. The following discussion summarizes the five steps of the modified BP algorithm.

Step 1: Input a packet, and check CRC. If pass, then translate the index to CI by lookup in the CIT.

Step 2: If the input packet is a degree one packet which has not yet been decoded, place it in the NRP memory. Otherwise, place it in the UDP memory and XOR with any previously decoded packets in the DP memory. This step may release new degree one packets, which are saved to the NRP memory, or reduce the degree of received packet.

Step 3: New released packets in the NRP memory are used to repeat Step 2 until no new degree one packets are released.

Step 4: Copy all NRP to the DP memory.

Step 5: If all k message packets are decoded in the DP memory, the decoding process stops. Otherwise, input a new packet and repeat Step 1.

2.4.3 Chain List of Raptor Decoder

To minimize the decoding time, the CI of undecoded packets must be recorded in a data structure which permits quick access. Define a *chain list* as an indexed set of lists, or *chains*, similar to a hash table with separate chaining. For example, to store the connection information for undecoded packets define a chain list CI_u in Fig. 2.7(a). Each UDP indexes a list containing the CI corresponding to the packet. By convention, the first entry in each chain is the degree of the packet and is set to ease implementation. Entries are made sequentially into CI_u each time a packet is added to the UDP memory. Though the degree of UDPs varies randomly, the size of the memory must be fixed. In this work, the depth of the chain list is set to the maximum degree in $\Omega(x)$. Once the degree of the UDP is reduced to one by the decoding algorithm it is moved to the NRP memory.

In order to avoid expensive searches through CI_u, another chain list CI_m is defined to hold the connection information of each message packet, as illustrated in Fig. 2.7(b). In CI_m, the k message packets index chains containing the set of UDPs which depend on the message packet. For example, from Fig. 2.7(b), UDPs A and B depend on message packet 1. Once the CI of a UDP is added to the CI_u, the index of this entry is also stored in every chain of CI_m connected to packet. For example, notice that packet A in CI_u in Fig. 2.7(a) is also contained in chains 1 and 3 of CI_m in Fig. 2.7(b).

To illustrate the operation of these chain lists, consider a case where the chain lists CI_u and CI_m are as in Fig. 2.7. Suppose a degree one packet is received containing message packet 2. Figure 2.8 illustrates the operation on the chain lists. First, CI_m is accessed indicating that UDP packets B and C depend on message packet 2. Then, chains B and C in CI_u are accessed, the degree is reduced by one and the reference to message packet 2 is removed. Finally, the chain for message packet 2 in CI_m is removed. In this way, the CI of remaining UDPs and message packets remains consistent and is easily accessed and modified.

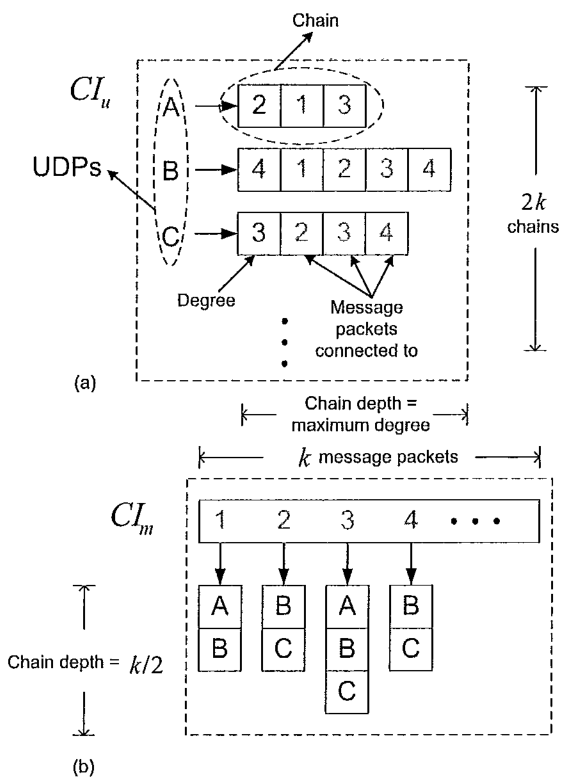

Figure 2.7: Structure of chain lists (a) CI_u and (b) CI_m

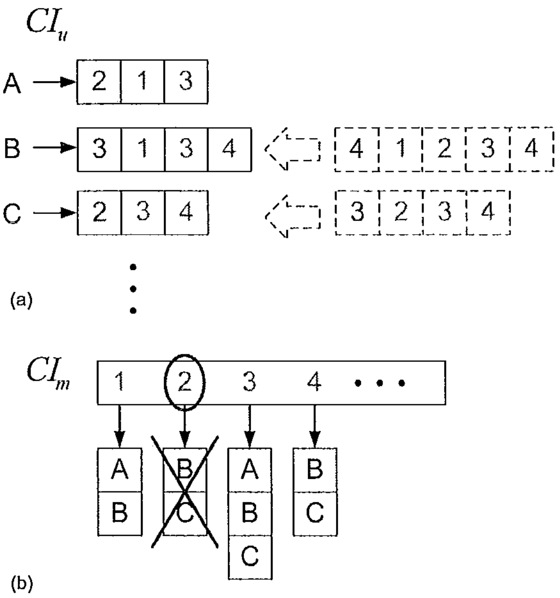

Figure 2.8: Example of chain list access

2.4.4 Time Analysis of Raptor Encoder and Decoder in Software

The decoding time of Raptor codes can be divided into two parts: the XOR operation on the data and chain list access to maintain interconnection information. Though CI_u and CI_m are accessed directly, update and deletion of chain list still costs time. In contrast, the operation of the encoder does not require chain list accesses and the encoding time is far smaller than decoding time. To get a rough estimate of the decoding speed for the Raptor codes designed in Sec. 2.3, the decode algorithm with chain lists is simulated for $k = 16 - 1024$ on a PC. In software, CI_u and CI_m are implemented in memory accessed by CPU. Each update of a chain list element at least contains "read", "assign value" and "write" command cycles. The PC has an AMD Athlon X2 3800+ CPU clocked at 2.0 GHz and the Dev-C++ complier was used for all simulations. The results of the simulation are shown as Fig. 2.9. Notice that as k increases the total decoding speed decreases quickly. The decoding rate of $k = 16$ reaches 1.3 Gbps, while that of $k = 1024$ drops to 50 Mbps. Limited by the chain list access, the average decoding time of every packet increases significantly with k. Also the larger d_{avg} for longer messages incurs more XOR operations. Though ε_m decreases with increasing k, from the discussion of Sec. 2.3.3, it is also clear that the decoding complexity increases significantly. Thus, for the high data rate FSO channels considered here, Gbps performance is only available from short-length Raptor codes.

To select the size of the tables containing CI_u and CI_m, extensive simulations were conducted to avoid overflow. For CI_u, it is assumed that the maximum number of undecoded packets is $2k$, as shown in Fig. 2.7. For CI_m the length of the depth of each chain was set to $k/2$. After more than 10^9 runs, simulations indicate that on average the CI_u is only 23% filled and the CI_m is 46% full. No errors were encountered in the simulation nor were errors encountered for tables of this size in the hardware implementation in Sec. 2.4.7. Although the size of CI_u and CI_m is significant, it is still acceptable for small k.

The key advantage of chain list memory is that the decoder is able to access the CI for each packet at any decoding stage without the need to search through a buffer. Interconnection information can be used and updated dynamically. The CI_u memory is necessary for decoding since it contains the interconnection information of each UDP. Strictly the CI_m contains redundant information and is not necessary. However, it is vital to ensure high-speed operation and to avoid searching through all UDPs. The use of chain lists CI_u and CI_m occupy significant hardware resources and are suitable for short-length Raptor codes, however, they allow for high speed

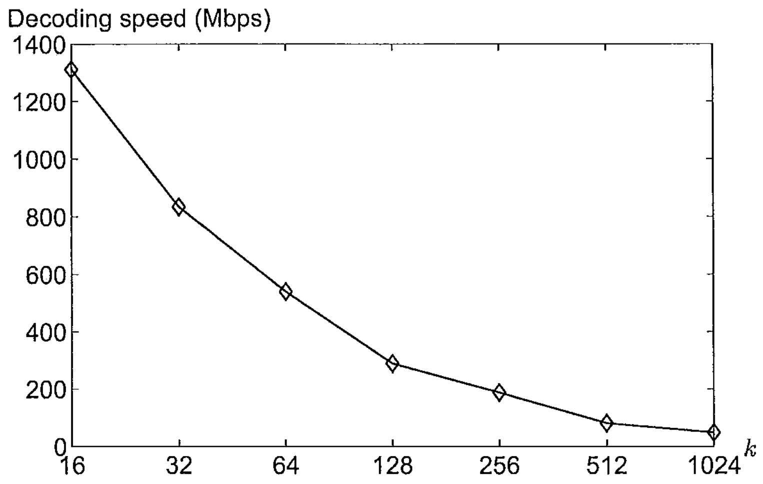

Figure 2.9: Software simulation estimate of decoding speed of Raptor decoder (running on CPU clocked at 2 GHz)

operation. Section 2.4.7 quantifies the required resources for a $k = 16$ Raptor encoder and decoder operating at high rates.

2.4.5 Hardware Architecture of Raptor Encoder

Figure 2.10 presents the hardware architectures of the Raptor encoder for the designed $k = 16$ code. Several modules are included under the top level encoder design. The *index counter* is a counter which records the index of current packet in the CIT. The CIT is implemented a 64 kbit ROM in the design. The *XOR Unit* can add two packets in each clock cycle. The *degree* signal controls the the number of XOR operations required. The *Central Logic* block is a finite state machine to arrange the actions of other modules for different encoding steps.

Signals of the Raptor encoder are listed in Tbl. 2.3. The primary challenge in designing the encoder is that each encoded packet requires a different number of operations due to its random degree. The Central Logic unit coordinates data access

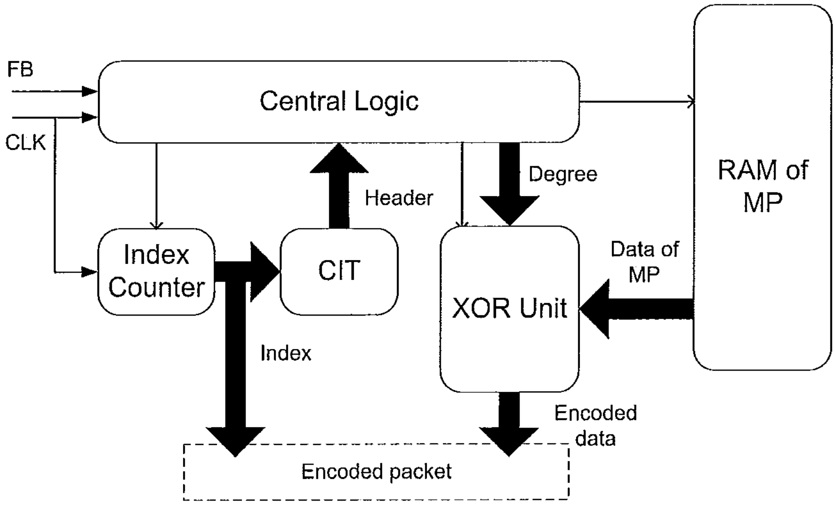

Figure 2.10: Architecture of Raptor encoder (MP=message packet). Thin lines are control signals while thick lines indicate data paths.

Table 2.3: Signals of Raptor encoder

Name	Type	Description
CLK	Input	Input clock signal
FB	Input	Feedback signal from decoder. If effective, encoding of current message is finished and Central Logic starts the next message.

to the message packet (MP) memory and XORs to ensure synchronous operation. The encoding process for a given message is stopped when the feedback (FB) signal is asserted and the Central Logic unit moves to the next message in the MP RAM.

2.4.6 Hardware Architecture of Raptor Decoder

From the previous discussion, it is clear that accesses to chain list dominate the decoding time when implemented in software. For this hardware design, however, CI_u and CI_m are both implemented with registers. This means that in one CLK

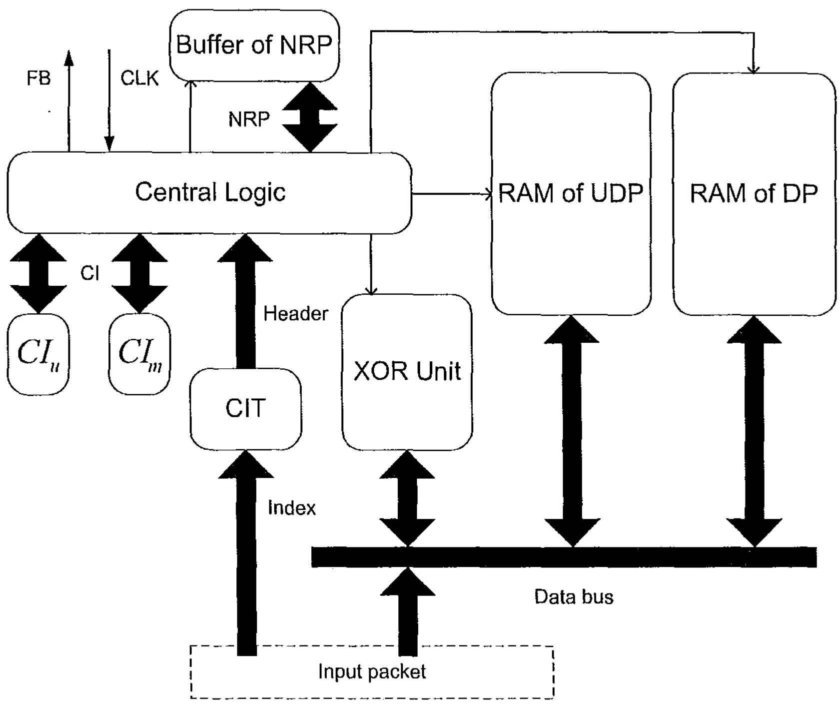

Figure 2.11: Architecture of Raptor decoder. Thin lines are control signals while thick lines indicate data paths.

cycle, update or deletion of any element in a chain can be finished. This is a pure hardware method to implement the chain list and in fact each chain is a circuit cell. The top level scheme of Raptor decoder is shown in Fig. 2.11. The CIT and XOR Unit modules of Raptor decoder are the same as the ones of encoder. The FB signal is an output signal of Raptor decoder and indicates when all message packets are decoded.

From Sec. 2.4.2, the undecoded, decoded and newly released packets are stored in separate memories. A data bus connecting these RAMs and XOR Unit is used. There are many access to RAM during the decoding process. For example, data of an undecoded packet is read first, then XORed by data of a decoded packet and written back to UDP RAM.

Table 2.4: FPGA Implementation results of Raptor encoder and decoder $k = 16$

	Encoder	Decoder
CLK frequency (MHz)	120	120
Data bus width (bit)	64	64
Equivalent gates	8230	26360
ROM size (kbit)	64	64
Power consumption (mW)	23	97
Required data RAM (kbit)	16 (MP)	32 (UDP)+16 (DP)
Speed (bps)	1.22 G	714 M

2.4.7 Hardware Implementation Result

The design of Raptor encoder and decoder is implemented in a Xilinx Virtex II-Pro XC2VP100 FPGA with ISE software [61, 62]. FPGA XC2VP100 is an advanced device with 130 nm technology and 10 million gates scale. Logic design implemented in XC2VP100 can be demonstrated by the high clock frequency at maximum 200 MHz. Average encoding and decoding speed of Raptor encoder are measured at maximum clock frequency at 120 MHz. Power consumption of the circuit is estimated through Xilinx XPE power estimate tool [63]. Details of implementation result are presented in Tbl. 2.4. Due to its simplicity, the speed of the encoder is faster than the decoder and thus, the Raptor decoder limits data rates of soft-switching hybrid FSO/RF systems. In this work, an FPGA hardware design achieves decoding speed as 714 Mbps with a 120 MHz clock.

Previous Raptor code implementations have been reported at several Gbps data rate on a 2.4 GHz Intel Xeon CPU, and 27 Mbps on a 206 MHz Intel StrongARM processor [35, 39]. Neither reference gives details on the code designed or its performance. However, such rates must be considered in light of the hardware complexity of such systems. In this work, the efficiency of the Raptor encoding and decoding algorithm has been demonstrated by the implementation in 2 GHz PC where decoding rate is up to 1.3 Gbps. Comparable data rates are realized using far simpler hardware at a much slower clock. In addition, the architecture is flexible and rates should scale with improved digital hardware implementations, i.e. FPGA or ASIC.

2.5 Conclusion

The short-length Raptor codes $(16-1024)$ in this chapter are designed with high rate and low decoding complexity. For $k = 1024$, $\varepsilon_m = 12\%$ and $d_{\text{avg}} = 6.32$. The reality of these codes is demonstrated by implementation in FPGA with 714 Mbps decoding speed, 26090 gates scale and 97 mW power consumption. In the following chapters, the designed short-length Raptor codes are applied to both hybrid RF/FSO channels as well as mobile FSO channels.

Chapter 3

Soft-Switching Hybrid FSO/RF Links using Raptor codes

In this chapter, for the hybrid FSO/RF links introduced in Chap. 1, the short-length Raptor codes designed in Chap. 2 are applied with a soft-switching scheme to maximize the total channel capacity.

Consider Fig. 3.1, a simple switching technique for hybrid links is to apply a hard-switching over these two links depending on received signal power as described in Chap. 1. However, only one link is selected while the other is sitting idle under a specific channel state. Further more, a great deal of feedback is needed to obtain channel state information at the transmitter. Since FSO and RF links can operate under very different data rates, frequent hard-switching over the two links costs system complexity. Short-length Raptor codes overcome the disadvantage of hard-switching by utilizing the capacity both of FSO and RF links simultaneously. Simulation results of the soft-switching performance of the short-length Raptor codes in three Canadian cities are presented in this chapter.

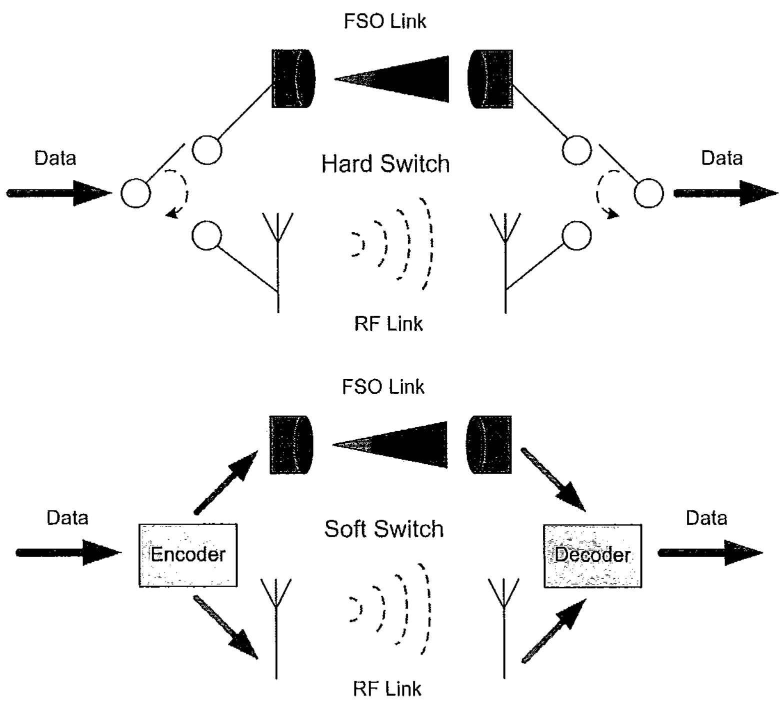

Figure 3.1: Hard and soft switching configurations for Hybrid FSO/RF links.

3.1 Hybrid FSO/RF Channel Model

For a point-to-point hybrid FSO/RF system in Fig. 3.1, the channel model is a combination of two individual line-of-sight (LOS) FSO and RF channels. In this section, details of these two channels described in Chap. 1 are presented.

3.1.1 FSO Channel

For an FSO link with OOK modulation, the channel model is defined as the same in (1.3). In this work of a stationary FSO link, the channel gain h is factored as [30],

$$h = h_l h_a h_g \tag{3.1}$$

where h_l, h_a and h_g denote the attenuation due to atmospheric loss, scintillation and geometric loss respectively. Since it is assumed that no sway of optical transmitter or receiver exists in this chapter, the misalignment loss $h_m = 1$ and is not considered here. Geometric loss, h_g, in this FSO channel model is a constant loss according to link parameters. Both h_l and h_a are time-variant, however, at very different time scales. The atmospheric loss h_l varies on the order of hours while scintillation varies on the order of $1 - 100$ ms [31]. This is in marked contrast to bit intervals which are typically 1 ns or less. The effect of h_a is a slow fading by which the FSO channel capacity is greatly impacted.

Atmospheric Loss

During propagation in free space, photons are absorbed and scattered by atmospheric particles, such as fog, rain and snow droplets. Generally, these particles have radii in a range 100 μm to 5000 μm [64] and cause varying attenuation depending on their distribution. The Beers-Lambert law defines h_l as,

$$h_l = e^{-\eta L} \tag{3.2}$$

where η is attenuation coefficient and L is propagation distance.

Because of the far smaller wavelength than RF links, atmospheric loss of FSO links is sensitive to water droplets such as fog. High loss up to 300 dB/km is possible for FSO links due to heavy fog [65]. When weather is clear and no droplet exists, loss can be less than 1 dB/km [66]. Atmospheric loss varies significantly under different weather conditions. For the purpose of this work, the attenuation coefficient will be modeled differently for the following weather conditions: clear/fog, rain and snow.

The appropriate model for η varies depending on the presence of precipitation and measured visibility data. Visibility is typically defined as the distance at which the transmitted optical intensity is attenuated to 2% of its original value [64]. In the case with no precipitation, e.g., clear or foggy weather, Kim's model is employed as [64],

$$\eta_{\text{no-precip}} = \frac{3.91}{V}\left(\frac{\lambda}{550}\right)^{-q} \tag{3.3}$$

where V is visibility in km, λ is wavelength in nm and q is a parameter related to the size distribution of particles,

$$q = \begin{cases} 1.6 \quad (V > 50 \text{ km}) \\ 1.3 \quad (6 \text{ km} < V < 50 \text{ km}) \\ 0.16V + 0.34 \quad (1 \text{ km} < V < 6 \text{ km}) \\ V - 0.5 \quad (0.5 \text{ km} < V < 1 \text{ km}) \\ 0 \quad (V < 0.5 \text{ km}) \end{cases} .$$

Atmospheric loss h_l for different visibility V is presented in Tbl. 3.1. On the basis of much experimental work, the loss determined by visibility is convincing and convenient to use [67–69]. However, this model is only accurate for a narrow wavelength range suitable for FSO communications, i.e. $\lambda = 785 - 1550$ nm [64]. In the case of precipitation, since the droplet size is far bigger than fog droplet, the loss is relatively wavelength insensitive. For rain, an accepted empirical model from [67] is,

$$\eta_{\text{rain}} = \frac{2.9}{V}. \tag{3.4}$$

For snow, the attenuation can be more severe due to a much larger droplet size. For a fair comparison with rain, following [70], η_{snow} is selected as,

$$\eta_{\text{snow}} = 20\eta_{\text{rain}}. \tag{3.5}$$

Notice that for rain and snow, only empirical models of loss are available. There exist more complex models of rain and snow attenuation which take visibility, temperature and droplet size into account. However, in this work, the simple models are adopted since only visibility data are available. Experimental results show these models are reasonably accurate in most cases [68, 71–73].

Scintillation

Atmospheric scintillation arises due to random changes in the refractive index of air along the transmission path. These refractive index changes introduce fading which varies on time scales of $1 - 100$ ms [31]. In every fading interval, an independent gain, h_a, is selected according to the Gamma-Gamma distribution [74],

$$\Pr(h_a) = \frac{2(\alpha\beta)^{(\alpha+\beta)/2}}{\Gamma(\alpha)\Gamma(\beta)}(h_a)^{\frac{(\alpha+\beta)}{2}-1}K_{\alpha-\beta}(2\sqrt{\alpha\beta h_a}) \tag{3.6}$$

where $K_{\alpha-\beta}(\cdot)$ is the modified Bessel function of the second kind and $1/\alpha$, $1/\beta$ are variances of large and small scale eddies respectively [74]. These two variances are related to the Rytov variance which represents the total intensity of atmospheric turbulence,

$$\eta_R^2 = 1.23\left(\frac{2\pi}{\lambda}\right)^{7/6} C_n^2\ L^{11/6} \tag{3.7}$$

where C_n^2 is the refractive-index structure parameter which is an air turbulence index denoting the atmospheric state independent of optical wavelength and L is the communication distance. Rytov variance η_R^2 is used to describe α and β through the expressions [74, pp.335-336],

$$\begin{aligned} 1/\alpha &= e^{0.49\ \eta_R^2/(1+1.11\ \eta_R^{12/5})^{7/6}} - 1, \\ 1/\beta &= e^{0.51\ \eta_R^2/(1+0.69\ \eta_R^{12/5})^{5/6}} - 1. \end{aligned} \tag{3.8}$$

The structure parameter, C_n^2, is the main parameter of the Gamma-Gamma distribution and represents the atmospheric turbulence level. Table 3.1 presents values for

Table 3.1: C_n^2 for different weather conditions

Weather Condition	$C_n^2 \times 10^{-14}$ ($m^{-2/3}$)	V (km)	h_l (dm/km, for $\lambda = 1550$ nm)
Clear	2	> 10	< 0.44
Light Haze	1.8	4–10	1.51–0.44
Haze	1.5	2–4	4.29–1.51
Thin fog	1	1–2	10.11–4.29
Light fog	0.5	< 1	> 10.11

C_n^2 for a variety of weather conditions used in this work [66, 75, 76]. Both C_n^2 and h_l may vary according to different atmospheric particle distributions under different conditions. Notice that turbulence is more severe in clear conditions than in foggy, high loss, conditions.

Geometric Loss

Geometric loss arises due to divergence of the transmitted beam and increases with propagation distance. For a fixed point-to-point link, assuming perfect alignment between transmitter and receiver exists and Gaussian beam profiles, the geometric loss can be approximated as,

$$h_g = \left[\mathrm{erf}\left(\frac{\sqrt{\pi}a}{\sqrt{2}w}\right)\right]^2, \quad w \approx L \cdot \phi \tag{3.9}$$

where w is the beam width at propagation distance L, $2a$ is the aperture diameter and ϕ is the divergence angle of beam [30]. The geometric loss h_g is a fixed loss for a given FSO link independent of weather conditions.

3.1.2 RF Channel

An IEEE 802.16 WiMAX point-to-point RF link operating at 5.8 GHz with 64-QAM modulation is considered as a complimentary link to the FSO channel [77, 78]. The 5.8 GHz band is relatively insensitive to deep rain fades [79]. In addition, the requirement of a line-of-sight for FSO implies that multipath distortion of the directive point-to-point RF link will be small. As a result, in this work the RF channel is modeled as an additive white Gaussian noise (AWGN) channel and only directive and antenna gains are considered.

Define the RF transmitted power as P_{RF} and the total channel gain of power as G_{RF},

$$G_{\mathrm{RF}} = G_{\mathrm{tx}} G_d G_{\mathrm{rx}} \tag{3.10}$$

where G_{tx}, G_{rx} are the antenna gains of the transmitter and receiver with respect to an isotropic antenna and G_d is the directive gain of isotropic antenna [80]. Highly directive RF antennas are available for the WiMAX standard with G_{tx} and G_{rx} in a range 10 dBi to 30 dBi [81]. Thus, for point-to-point applications, WiMAX RF links achieve several km transmission distances at rates of tens to hundreds of Mbps [77, 82]. In addition, with the 20 MHz bandwidth, the maximum communication distance of commercial WiMAX systems reaches $7-50$ km [77, 83]. For short distance $0.5-2$ km, the AWGN channel model for WiMAX link is realistic.

3.2 Raptor Coded Soft-Switching Hybrid FSO/RF Channel

3.2.1 Packet-Level Raptor codes

The previous discussion on channel modelling considers the channel at discrete signalling intervals. A common technique is to collect groups of transmitted bits into packets for transmission over the channel. This packetization of bits is practical and required for such high-speed links since processing at the packet-level is far less onerous than signal processing at the bit-rate, especially for links approaching Gbps rates.

In the remainder of this chapter, transmitting packets of ℓ bits over FSO or RF channels is considered. Figure 3.2 presents a diagram and the combined channel. Note, the channel model is applied to every bit, however, processing is done on each packet. Also, hard detection is only considered at the receiver to keep complexity realistic. In order to ensure reliable communications, a cyclic-redundancy code (CRC) is applied to each packet to detect any errors. After the CRC encoding, Raptor packets in bitstream are sent to OOK and 64-QAM modulation respectively. Binary bits in an encoded Raptor packet are mapped to OOK for each bit in FSO link and to 64-QAM for every 6 bits in RF link. Demodulation and decoding at receiver are in the inverse process as transmitter. Examples of such codes include 32-bit CRC from the IEEE 802.3 standard [84] which has efficient implementations for encoding and decoding at high speeds. For this example, it has been shown that the probability of undetectable error is $< 10^{-9}$, when bit error probability < 0.5 [84]. As a result, any corrupted packets are discarded by the receiver and end-to-end channel for FSO or

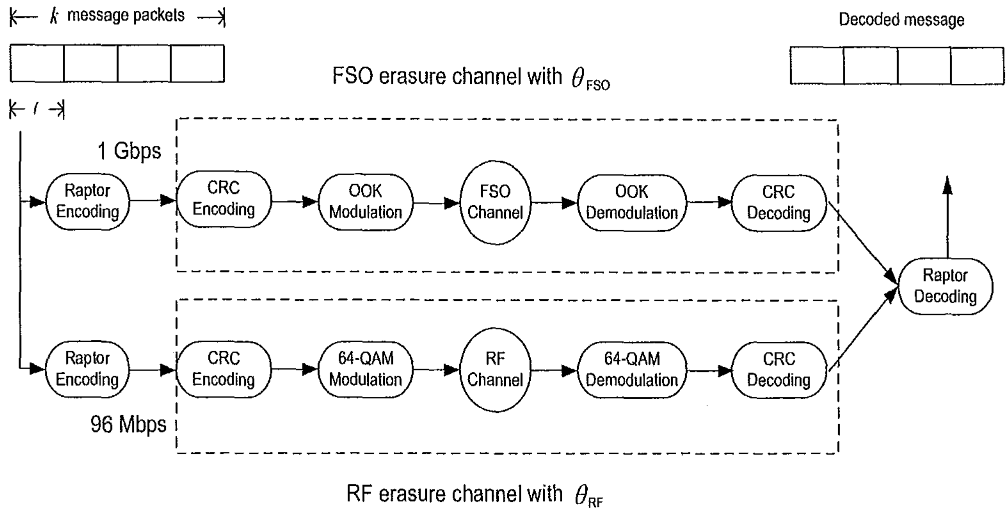

Figure 3.2: Combined channel model of the soft-switching hybrid FSO/RF link

RF links is a packet erasure channel. The packet erasure probability of FSO and RF channel are θ_{FSO} and θ_{RF} respectively. In the following section, a packet-level coding technique to achieve efficient soft-switching in hybrid FSO/RF links is described.

3.2.2 Simulation Setup

From the channel model described in Sec. 3.1, it is known that data rate of the FSO channel is affected by weather condition significantly. During fog conditions, the intensity of the optical signal is greatly attenuated, following (3.3). Additionally, rain and snow also severely attenuate transmissions according to (3.4) and (3.5). Even in clear conditions, the optical power is still impacted by scintillation according to (3.6). In the simulations, OOK modulation is assumed with hard decision decoding for every bit in the packet. The channel gain of a specific fading coherence time is fixed and it is assumed that the receiver knows exactly the channel gain for a bit-wise detection. The threshold of bit-wise hard detection is determined by the channel gain. In practice, an AGC is used to integrate the received signal for detection as mentioned in Chap. 1.

After application of the CRC, the effective channel for both RF and FSO links is an erasure channel. Since Raptor codes are applied, an increase in θ_{FSO} due to atmospheric conditions will cause the decoded data rate to scale down appropriately. The WiMAX RF channel working at 5.8 GHz has a lower data rate but is more far more stable than FSO channel over weather conditions. In well designed point-to-point systems, the impact of fading and noise at this RF frequency are small. With a lower transmission rate, the WiMAX RF link can be recognized as a backup of FSO link. The parameters of the FSO and RF link for simulation are presented in Tbl. 3.2 and are chosen from [5, 75, 77, 85]. Since the 5.8 GHz frequency is an unlicenced band in WiMAX standard applied by many commercial systems, the 96 Mbps is chosen as the highest rate at this frequency from a commercial link [77]. Other link parameters such as antenna gain is also chosen from the commercial link [77]. Parameters of the FSO link are chosen from the fSONA system which is one of the most highest data rate commercial FSO links available in the world [5]. The selection of these highest data rates of FSO and RF links is meaningful because they represent the newest technology of both the links. However, even for the newest technology, data rate of the FSO link is much faster than that of the RF link.

The simulations are based on 2007 climate data from [86]. Since only hourly data is available, it is assumed that atmospheric parameters C_n^2 and V do not change within an hour. The coherence time of optical scintillation is taken to be 10 ms from [31]. In every coherence interval, a channel gain h_a due to scintillation is generated according to (3.6). Practical link distances, $L = 0.5$, 1 and 2 km are simulated. In

Table 3.2: Parameters of the FSO and RF link for simulation

FSO link		
Parameter	Symbol	Value
Wavelength	λ	1550 nm
Transmission rate	ξ_{FSO}	1 Gbps
Transmitted power	P_{FSO}	320 mW
Receiver responsivity	R	0.5 A/W
Variance of noise	N_{FSO}	10^{-14} A^2
Laser divergence angle	ϕ	2 mrad
Receiver diameter	$2a$	20 cm
RF link		
Parameter	Symbol	Value
Frequency	f	5.8 GHz
Transmission rate	ξ_{RF}	96 Mbps
Transmitted power	P_{RF}	16 mW
Bandwidth	B	20 MHz
Variance of noise	N_{RF}	10^{-10} mW
Antenna gain of transmitter	G_{tx}	16 dBi
Antenna gain of receiver	G_{rx}	30.4 dBi

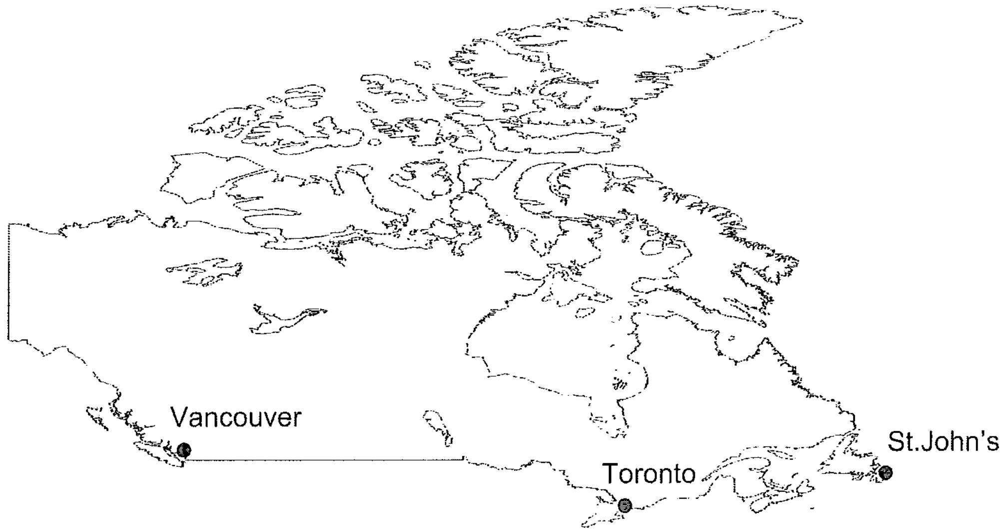

Figure 3.3: Location simulation sites: Vancouver, Toronto and St. John's, Canada

all cases, it is assumed that the LOS links are placed in stationary locations and the initial alignment between transmitter and receiver is assured.

Simulations are also performed for climate data for three Canadian cities: Vancouver, Toronto and St. John's. These cities are located in west coast, south border and east coast of the country respectively, as shown in Fig. 3.3. All of cites are located at latitudes of $49^o - 43^o$ North. The climate of Vancouver is moderate oceanic, where most rainfall occurs in winter. Toronto has a humid continental climate, where summer is warm and rainy, and winter is cold and snowy. From an FSO communications perspective, St. John's has the most challenging climate. In a large portion of a year, it is foggy, cloudy or snowy. For example, on average St. John's experiences 126 days of fog per year [87]. St. John's is also affected by tropical storms from the Atlantic Ocean.

Simulations are conducted for hybrid FSO/RF links with hard-switching and soft-switching with the designed short-length Raptor codes with message lengths $k = 16$

and 1024. Although the $k = 16$ case is practical and less complex, it has a much higher overhead than $k = 1024$ code as presented in Fig. 2.5. For hard-switching, a reasonable technique from literature [46] is adopted. It is assumed that in each coherence interval of 10 ms, the hard-switching system can detect the instantaneous received optical power. If the received power is 3 dB over the threshold to get 10^{-9} BER, the FSO link is selected, otherwise, the RF link is selected [46]. Notice that the hard-switching is a complex scheme requiring significant feedback and channel estimation.

3.2.3 Simulation Results on Average Data Rate

Average daily data rates are simulated for three link ranges in the three target cities using a variety of hard- and soft-switching techniques. Figures 3.4-3.12 present the daily average data rates for the three cites. The average daily data rates over the year for different link ranges and locations are also presented in Tbl. 3.3. From the three figures it is apparent that the data rates vary significantly depending on the time of year. Typically, high rates are available in summer months while low rates occur in winter months due to snow, rain and fog conditions. The temperate climate of Vancouver gives rise to less variation in rates than Toronto or St. John's.

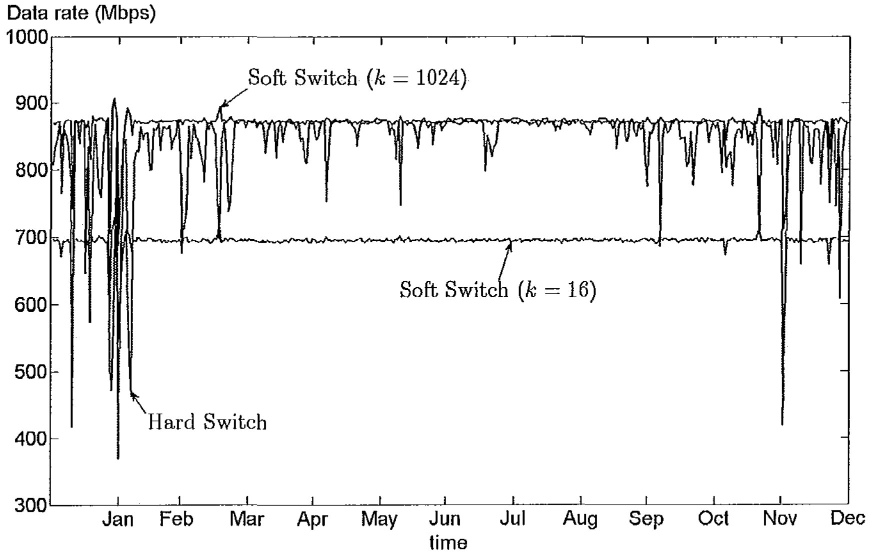

Figure 3.4: Daily average data rates in Vancouver $L = 0.5$ km

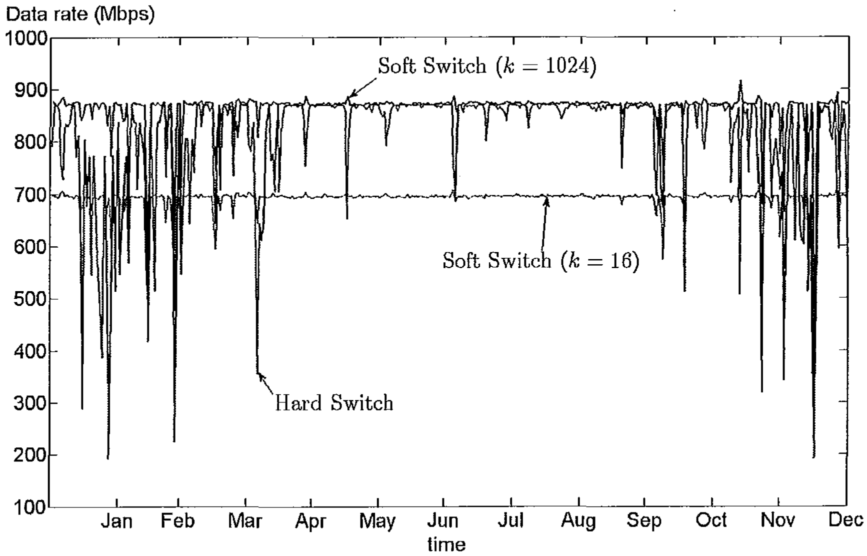

Figure 3.5: Daily average data rates in Toronto $L = 0.5$ km

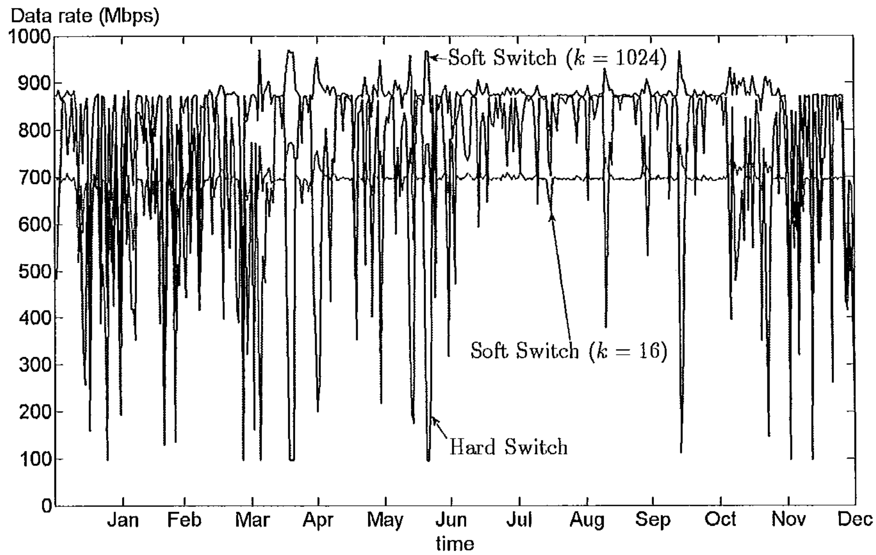

Figure 3.6: Daily average data rates in St. John's $L = 0.5$ km

In all cases, at $L = 1$ km the soft-switching Raptor codes outperform hard-switching. However, from Tbl. 3.3, when $L = 0.5$ km the optical power is high enough to achieve the required BER and little hard-switching occurs. In this case, due to the overhead of the Raptor code ε_m, CRC and index, the data rates of soft-switching $k = 16$ Raptor codes is lower. However, the lower overhead of $k = 1024$ Raptor codes does realize a gain in average rate. For longer range links, $L = 1$ and 2 km, the optical power is reduced by loss and scintillation significantly. Hard-switching turns to the backup RF link frequently, wasting any available FSO data rate, and causes a total data rate decrease. Soft-switching with Raptor codes achieves a much higher data rates for these 2 cases. The $k = 16$ Raptor code improves data rate from 100 Mbps level of hard-switching to 400 Mbps. This data rate is easily supported by the 714 Mbps rate of the implemented decoder in Sec. 2.4. Although a practical high-speed decoder for $k = 1024$ is not presented in this thesis, it is an interesting

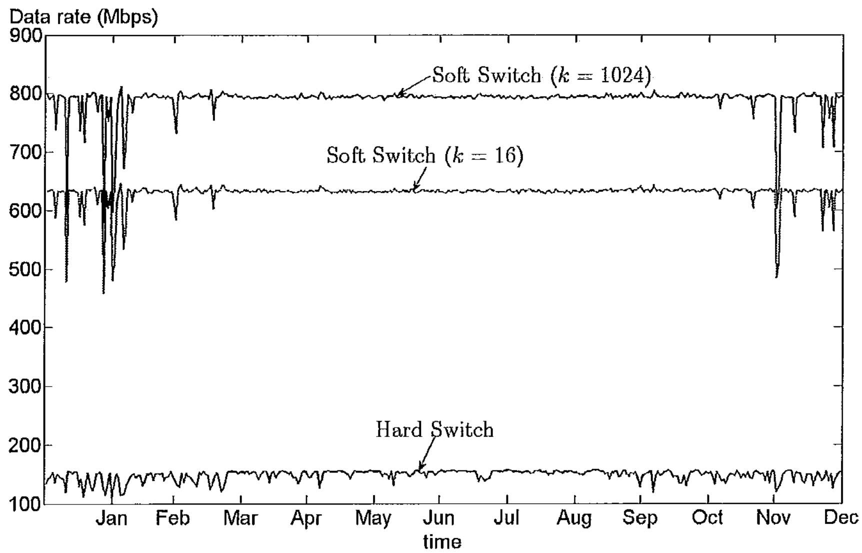

Figure 3.7: Daily average data rates in Vancouver $L = 1$ km

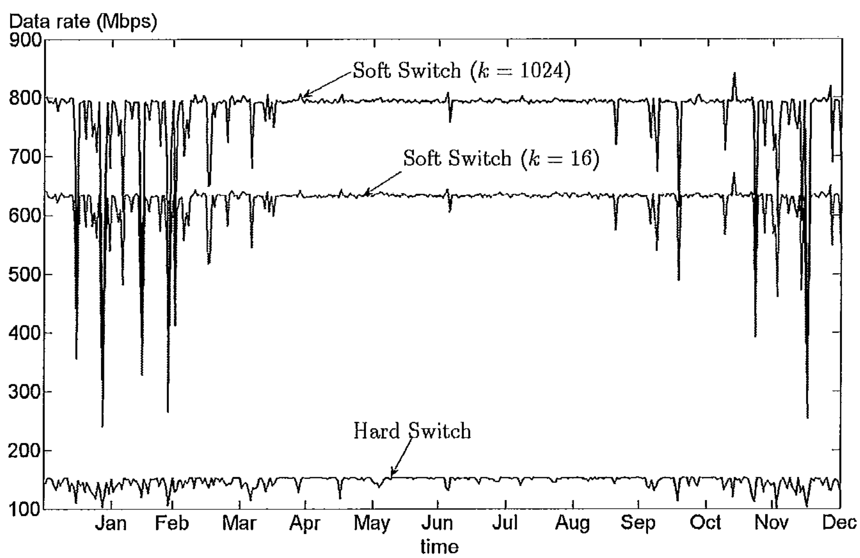

Figure 3.8: Daily average data rates in Toronto $L = 1$ km

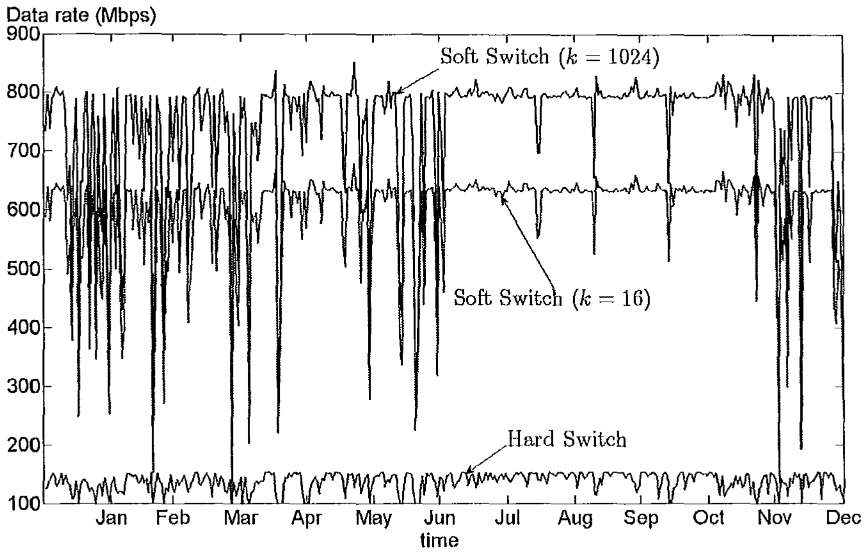

Figure 3.9: Daily average data rates in St. John's $L = 1$ km

future direction due to the higher supported rates.

The key advantage of soft-switching is that loss and scintillation need not be considered at the transmitter directly. No matter the weather condition, soft-switching based on short-length Raptor codes can achieves a high data rate according to erasure probability of the underlying channel. Compared to hard-switching, soft-switching with Raptor codes avoids the disadvantage of frequently switching between FSO and RF link. Also, soft-switching utilizes both FSO and RF links simultaneously increasing the efficiency over hard-switching and needs much less feedback. Soft-switching offers trade off of more average data rate for some coding overhead.

3.2.4 Simulation Results on Reliability

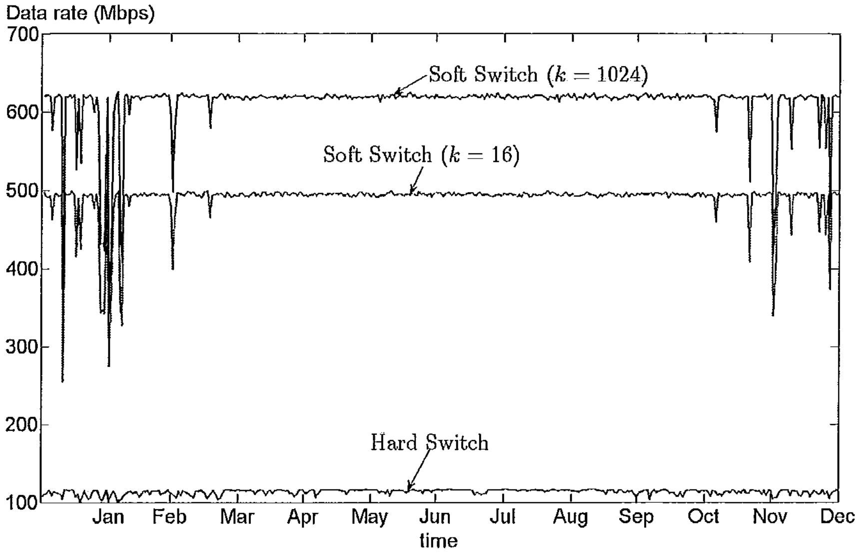

Figure 3.10: Daily average data rates in Vancouver $L = 2$ km

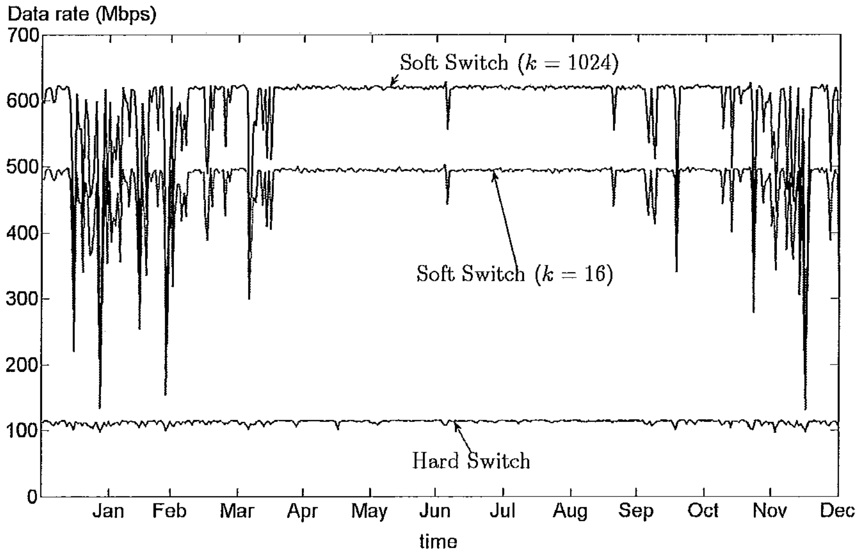

Figure 3.11: Daily average data rates in Toronto $L = 2$ km

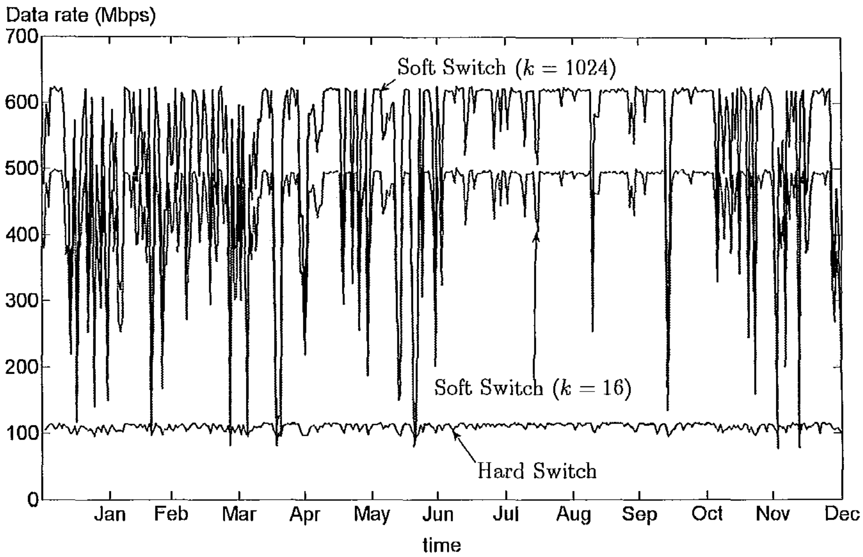

Figure 3.12: Daily average data rates in St. John's $L = 2$ km

Table 3.3: Simulation result of average daily data rates

Vancouver (Mbps)			
	$L = 0.5$ km	$L = 1$ km	$L = 2$ km
Soft switch ($k = 1024$)	869.3	788.5	610.9
Soft switch ($k = 16$)	692.8	628.4	487.6
hard-switching	839.4	147.6	113.0
Toronto (Mbps)			
	$L = 0.5$ km	$L = 1$ km	$L = 2$ km
Soft switch ($k = 1024$)	862.3	774.2	590.9
Soft switch ($k = 16$)	687.0	617.6	472.0
hard-switching	803.4	145.8	112.4
St.John's (Mbps)			
	$L = 0.5$ km	$L = 1$ km	$L = 2$ km
Soft switch ($k = 1024$)	846.8	737.2	538.9
Soft switch ($k = 16$)	674.7	587.9	430.7
hard-switching	689.8	136.6	109.4

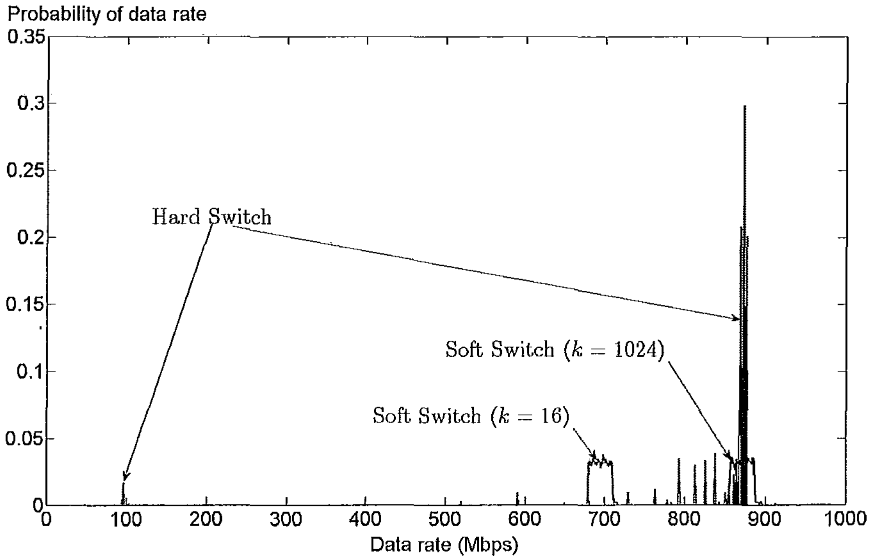

Figure 3.13: Distribution of average hourly data rate for soft-switching hybrid FSO/RF link in Vancouver $L = 0.5$ km

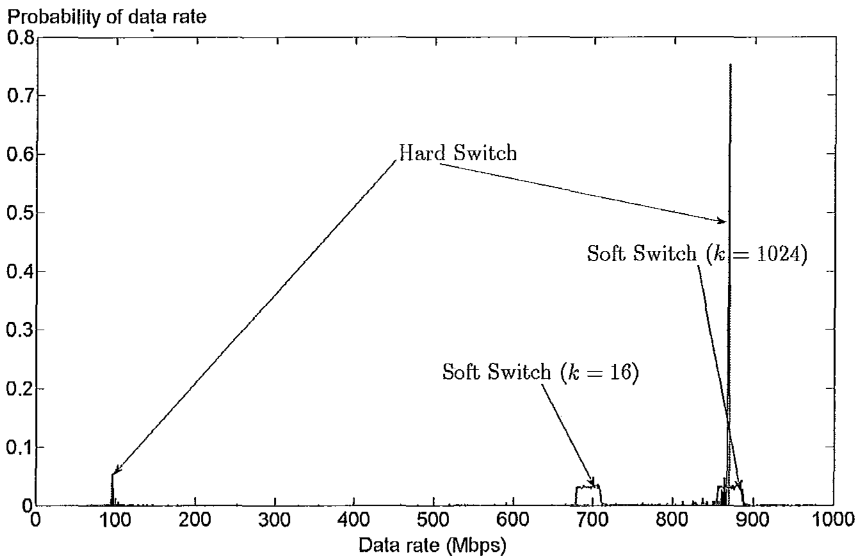

Figure 3.14: Distribution of average hourly data rate for soft-switching hybrid FSO/RF link in Toronto $L = 0.5$ km

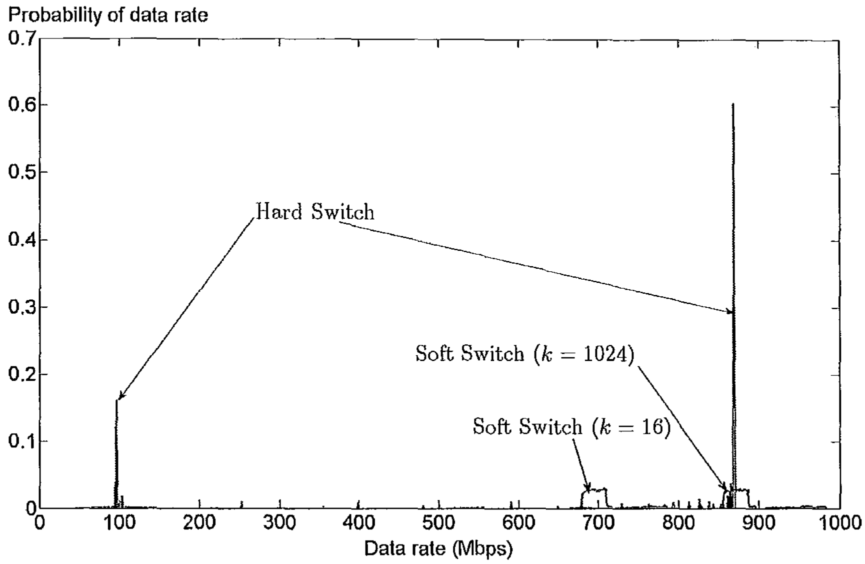

Figure 3.15: Distribution of average hourly data rate for soft-switching hybrid FSO/RF link in St. John's $L = 0.5$ km

From Fig. 3.13-3.21, the data rate distributions of the hard- and soft-switching in the three Canadian cities are presented. Notice that in the case of hard-switching, the distributions are dominated two large peaks indicating that either RF or FSO links are selected. In contrast, the soft-switching hybrid FSO/RF channels have larger average rates and are able to exploit both channels simultaneously. The soft-switching schemes have a larger variance in data rate than the hard-switching due to the ability of the Raptor codes to adapt to the variable channel conditions. This in turn may incur some additional complexity due to the adaptive rate of the channel which is compensated by the larger available rates.

Define reliability of the hybrid system as the probability that the data rate is greater than a given value R_0 as,

$$\text{Reliability} = \Pr(\text{data rate} \geq R_0) \times 100\% \tag{3.11}$$

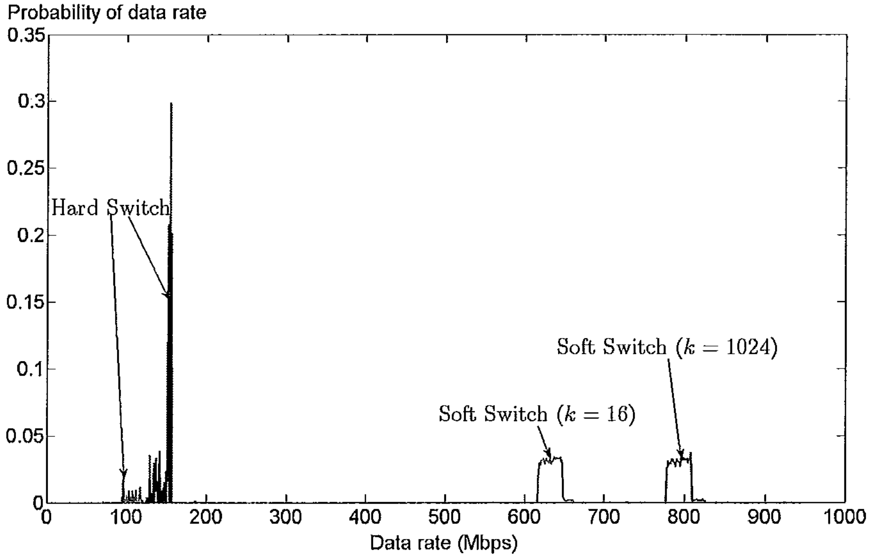

Figure 3.16: Distribution of average hourly data rate for soft-switching hybrid FSO/RF link in Vancouver $L = 1$ km

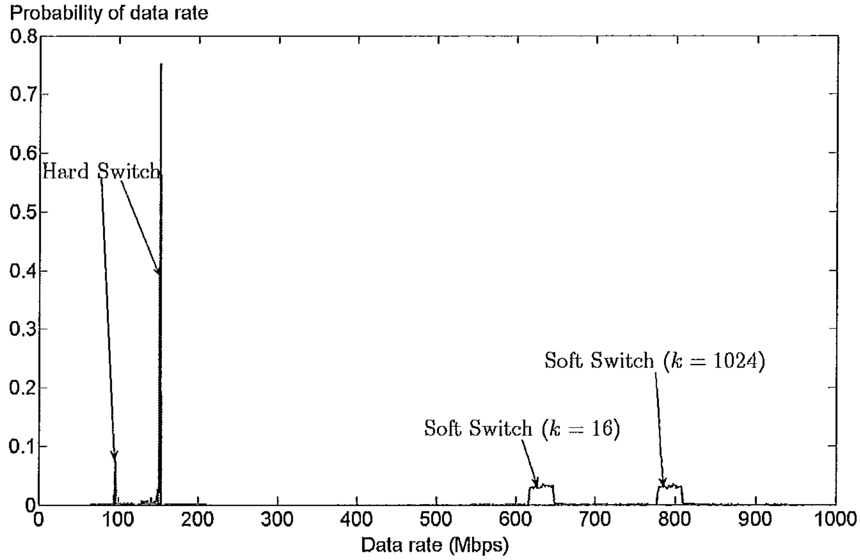

Figure 3.17: Distribution of average hourly data rate for soft-switching hybrid FSO/RF link in Toronto $L = 1$ km

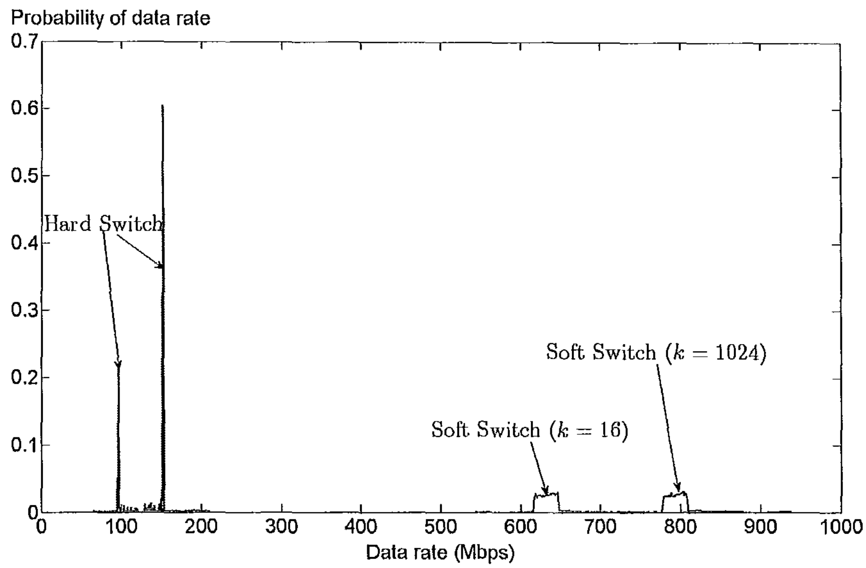

Figure 3.18: Distribution of average hourly data rate for soft-switching hybrid FSO/RF link in St. John's $L = 1$ km

The R_0 corresponding to 99%, 99.9% and 99.99% reliability of the year are presented respectively in Tbl. 3.4. For hard-switching, the high reliability $\geq$ 99% is the case that the RF link is selected and the data rate is close to RF transmission rate 96 Mbps. However, for soft-switching cases, due to a higher usage both through the two links, total data rate is more flexible than hard-switching. The rates for a given reliability level are lower with soft-switching than hard-switching. This is due to the larger range of data rate as well as the overhead of the code. However, this small loss in reliability is compensated by the a large increase of average data rate. Thus, soft-switching gives a trade-off of slighty lower reliability for a larger average data rate.

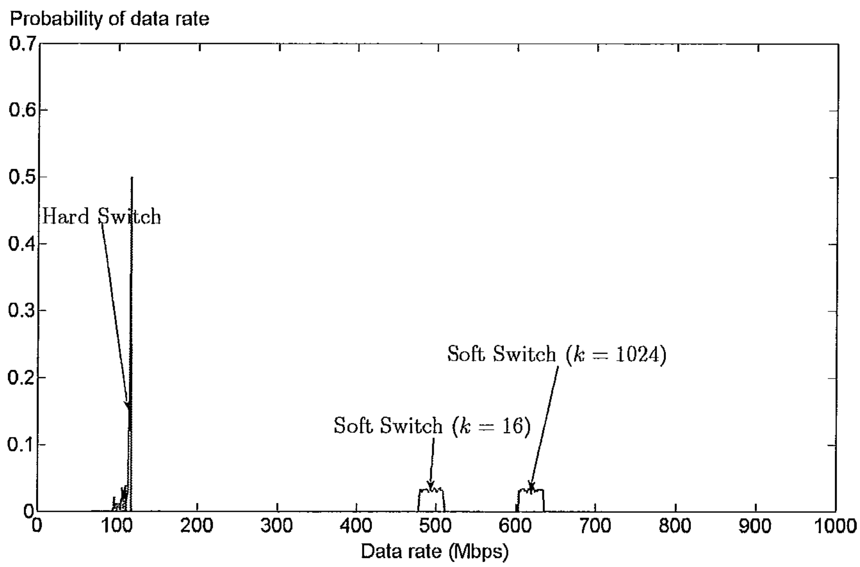

Figure 3.19: Distribution of average hourly data rate for soft-switching hybrid FSO/RF link in Vancouver $L = 2$ km

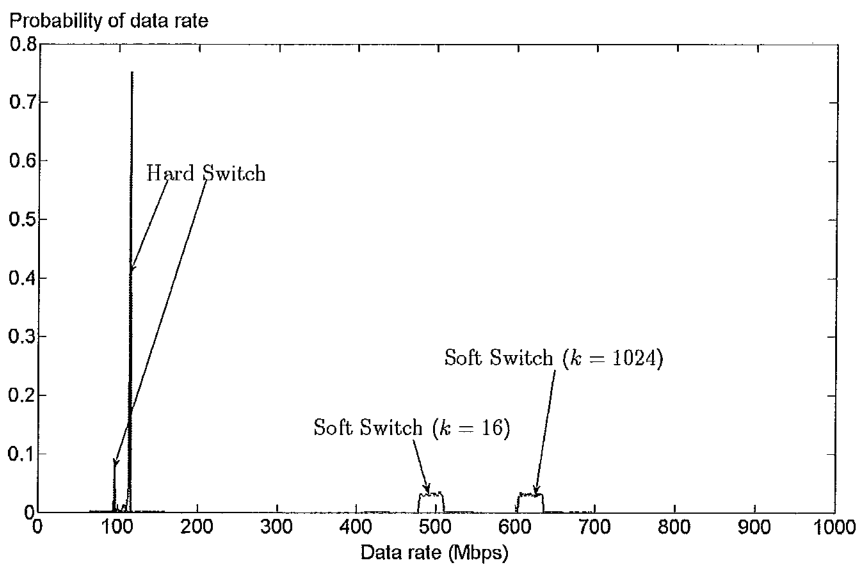

Figure 3.20: Distribution of average hourly data rate for soft-switching hybrid FSO/RF link in Toronto $L = 2$ km

Table 3.4: Simulation of data rate, R_0, for different reliabilities

(Mbps)	99%	99.9%	99.99%	Average rate
Vancouver $L = 0.5$ km				
Soft switch ($k = 1024$)	96	84	84	869.3
Soft switch ($k = 16$)	79	66	66	692.3
hard-switching	97	97	97	839.4
Toronto $L = 0.5$ km				
Soft switch ($k = 1024$)	94	83	82	862.3
Soft switch ($k = 16$)	79	66	66	687.0
hard-switching	97	97	97	803.4
St. John's $L = 0.5$ km				
Soft switch ($k = 1024$)	93	83	81	846.8
Soft switch ($k = 16$)	76	66	64	674.7
hard-switching	97	97	97	689.8
Vancouver $L = 1$ km				
Soft switch ($k = 1024$)	94	82	82	788.5
Soft switch ($k = 16$)	75	66	66	628.4
hard-switching	96	96	96	147.6
Toronto $L = 1$ km				
Soft switch ($k = 1024$)	92	81	80	774.2
Soft switch ($k = 16$)	75	66	65	617.6
hard-switching	96	96	96	145.8
St. John's $L = 1$ km				
Soft switch ($k = 1024$)	90	82	81	737.2
Soft switch ($k = 16$)	73	66	64	587.9
hard-switching	96	96	96	136.6
Vancouver $L = 2$ km				
Soft switch ($k = 1024$)	92	81	81	610.9
Soft switch ($k = 16$)	73	66	65	487.6
hard-switching	96	96	96	113.0
Toronto $L = 2$ km				
Soft switch ($k = 1024$)	90	81	80	590.9
Soft switch ($k = 16$)	72	66	66	472.0
hard-switching	96	96	96	112.4
St. John's $L = 2$ km				
Soft switch ($k = 1024$)	83	82	82	538.9
Soft switch ($k = 16$)	66	66	64	430.7
hard-switching	96	96	96	109.4

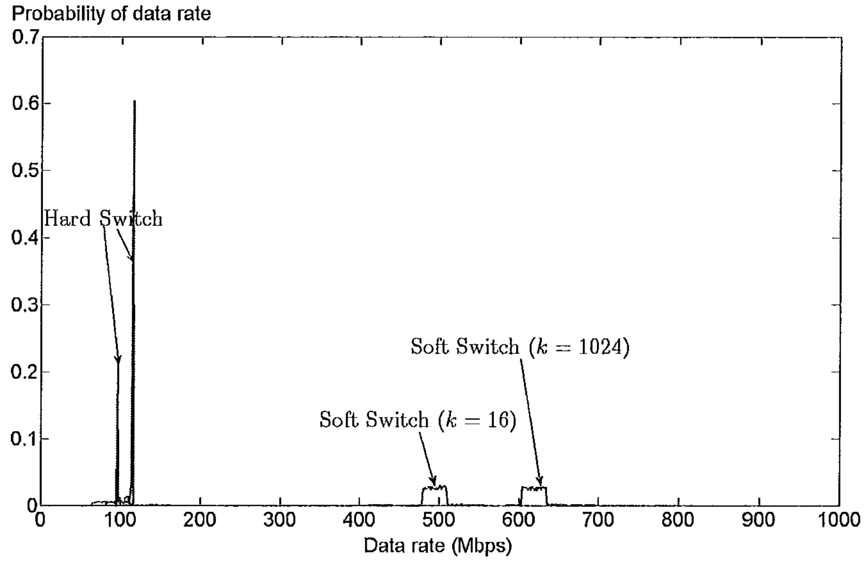

Figure 3.21: Distribution of average hourly data rate for soft-switching hybrid FSO/RF link in St. John'so $L = 2$ km

3.3 Conclusions

In this chapter, a soft-switching scheme for hybrid FSO/RF links with packet-level Raptor codes is proposed. To investigate the data rate of short-length Raptor codes in Chap.2 in a practical environment, parameters from a 1 Gbps FSO link and a 96 Mbps WiMAX RF link are used to simulate the hybrid FSO/RF link. Simulation under 2007 climate data of three Canadian cities shows that soft-switching with $k = 16$ Raptor code achieves average data rates of at least 430 Mbps for a transmission distance $L = 2$ km compared to 109 Mbps data rate for hard-switching. Thus, practical soft-switching hybrid FSO/RF links based on short-length Raptor codes are both practical and efficient in coordinating the simultaneous use of these channels.

Chapter 4

Short-Length Raptor Codes for Mobile FSO Links between UAV and Ground Station

As described in Chap. 1, a UAV is a high-speed aircraft which is piloted remotely. Two typical military UAVs in US airforce are the MQ-1 Predator and the RQ-4A/B Global Hawk [88, 89]. The maximum speed of Predator and Global Hawk is 220 km/h and 730 km/h respectively [90]. Russia also has super-sonic UAVs such as the Tu-143 unmanned reconnaissater which can reach speeds as high as 950 km/h [91]. Photos

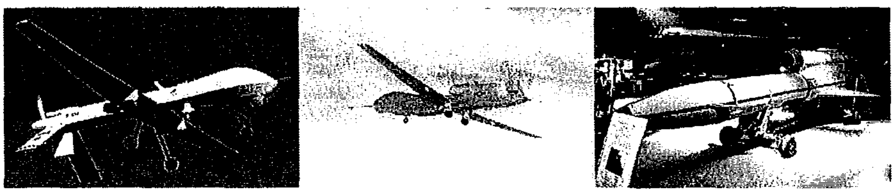

(a) (b) (c)

Figure 4.1: Typical UAVs: (a) Predator, (b) Global Hawk and (c) Tu-143 [88-90]

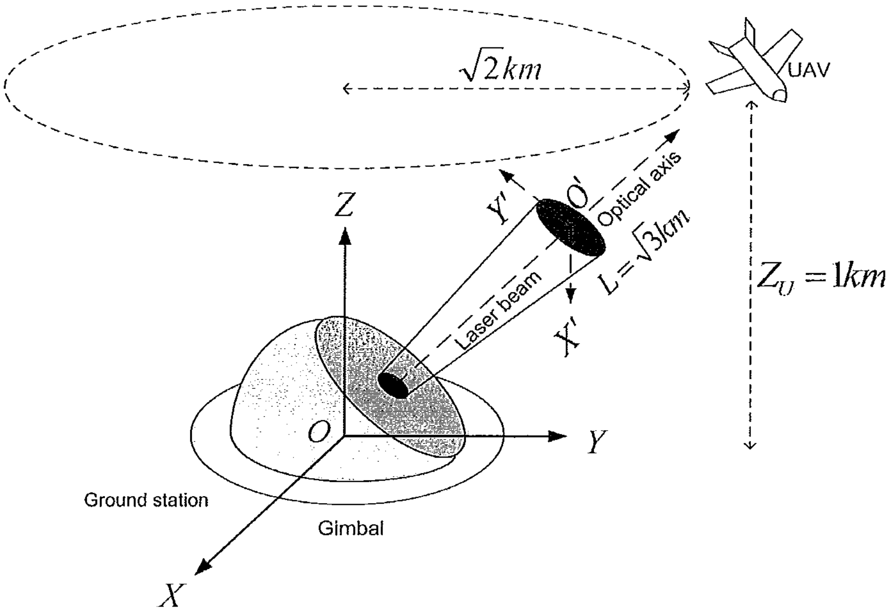

Figure 4.2: Ground-to-UAV Mobile FSO channel configuration

of these UAVs are presented in Fig. 4.1. Compared to RF links, FSO links offer higher data rate and security to the wireless communications of UAV. Also, mobile platforms such as UAV benefit from a lower system cost and weight of FSO than RF links. FSO links between UAV and ground station have been considered in previous work [52–54]. In this chapter, a ground-to-UAV FSO link is considered as presented in Fig. 4.2. However, this FSO link suffers from the severe misalignment due to the high-speed motion of the UAV. In this chapter, the short-length Raptor codes designed in Chap. 2 are applied in this channel and the performance of the codes are presented.

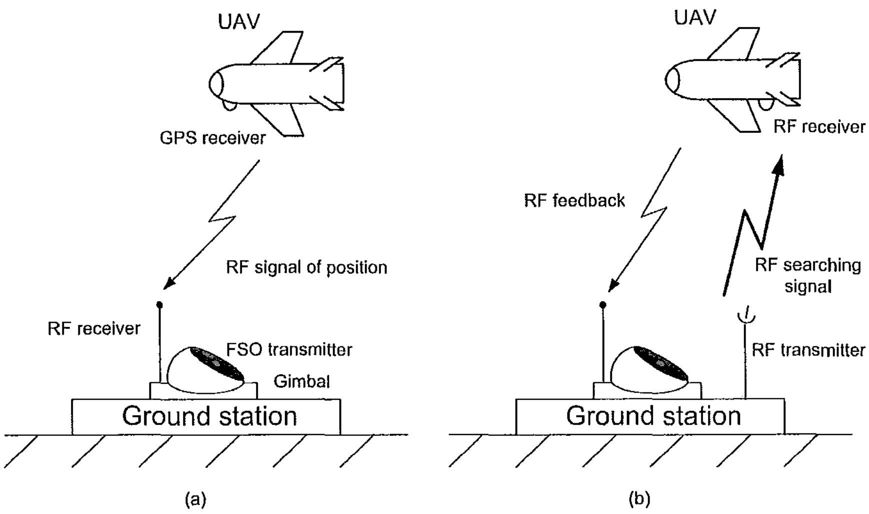

Figure 4.3: Two tracking systems of ground-to-UAV FSO links: (a), GPS tracking system and (b), RF tracking system

4.1 FSO Channel Model

Since the divergence of optical beam is much less than that of RF links, tracking these high-speed UAVs is the major problem for the ground-to-UAV FSO links. In general, UAVs can move randomly in 3 dimensions (3D) according to a tactical maneuver. Circling around a battlefield is a typical maneuver for such aircraft. In this case, UAVs fly in a stationary path with a stable speed. In this chapter, ground-to-UAV communication for a stationary path is considered.

Different tracking systems for UAVs have been developed in previous work. Two widely-used methods of tracking UAVs employ Global Positioning System (GPS) and RF tracking systems respectively as presented in Fig. 4.3 [92–94]. In Fig. 4.3 (a), for a GPS tracking system, a GPS receiver is installed on the UAV and the position information of the UAV is transmitted back to the ground station. In Fig. 4.3 (b), for an RF tracking system, an RF transmitter sends searching signal to the UAV and a feedback is sent back to the ground. The UAV position is calculated by the amplitude and the delay of the feedback signal. After the position of UAV is known, the ground station rotates the optical beam toward the UAV. Since RF tracking systems can be designed following specific requirements without any standards, the tracking performances of these systems vary widely. In this thesis, a GPS tracking system for the ground-to-UAV FSO link is considered. Following civil GPS standard a typical accuracy of 10 m for 2D and 16 m for 3D measurements. The *tracking interval* is the minimum duration where measurement is taken and is typically 50 ms [95–98]. These position updates occur slowly relative to the UAV motion and only small angle adjustments are needed for the optical beam due to a long communication distance.

In this chapter, the configuration of the tracking system is selected from previous research work of ground-to-UAV links as Fig. 4.2. This system includes a gimbal for rotating the laser transmitter in two dimensions and GPS for UAV position information [12]. A gimbal is a two-dimensional rotatable support where mechanical error of the pointing exists. Experimentally measured error of this tracking system are combined with error of GPS and gimbal and effects of atmospheric scintillation are considered in the channel model [12, 74]. Severe misalignment caused by UAV motion occurs even after the tracking system is employed. Short-length Raptor codes are applied to overcome the misalignment in this chapter.

As mentioned in [12], the gimbal is at the origin, O, of coordinate system XYZ in Fig. 4.2. A UAV flies in a $\sqrt{2}$ km circle at a speed of 100 m/s with altitude $Z_U = 1$ km, and the circle is parallel to plane XY. The ground-to-UAV distance along the optical axis is $L = \sqrt{3}$ km. Define the plane $X'Y'$ to be transverse to the optical axis. It is assumed, as in [12], that initial acquisition between UAV and base station has been completed before tracking. As in [12], the tracking process is performed periodically by updating the UAV position by GPS at a tracking interval T_{tr} and orienting the gimbal accordingly.

The channel model is the same as (1.1) with OOK modulation. The channel gain h can be factored as

$$h = h_l h_a \underbrace{h_g h_m}_{h_{tr}} \tag{4.1}$$

where h_l and h_a denote the attenuation due to atmospheric loss and scintillation respectively. And the geometric loss h_g and misalignment loss h_m due to motion defined in equation (1.4) are combined as h_{tr}.

4.1.1 Atmospheric Model

The propagation loss, h_l is defined as a deterministic function of a propagation distance L by Beer-Lambert Law

$$h_l(L) = e^{-\eta L}$$

where η is the scattering coefficient.

For atmospheric scintillation, h_a is a random fading coefficient due to scintillation. Different from Chap. 3, the uplink to UAV also includes the vertical path where atmospheric parameters such as wind speed, temperature and air pressure vary significantly. In order to model the distribution of h_a, an uplink Hufnagel-Valley model was applied to define the refractive-index structure parameter $C_n^2(Z)$ at different altitudes

Z as [74, p.481]

$$
\begin{aligned}
C_n^2(Z) =& 0.00594(s/27)^2(10^{-5}Z)^{10}e^{-Z/1000} \\
&+ 2.7 \times 10^{-16}e^{-Z/1500} + Ae^{-Z/100}
\end{aligned}
$$

where s is a speed of strong wind and A denotes a nominal ground turbulence level similar as C_n^2. Notice that in Chap. 3, C_n^2 is a constant chosen according to different weather conditions. In contrast, in this chapter for an uplink, after the ground turbulence level A is chosen, the vertical path is still highly impacted by wind speed s and decreasing air pressure represented by altitude Z. Secondly, for laser wave-length $\lambda = 1550$ nm, an intermediate constant σ_{Bu}^2 is calculated from $C_n^2(Z)$ [74, p.509].

$$
\sigma_{Bu}^2 = 2.25\left(\frac{2\pi}{\lambda}\right)^{\frac{7}{6}}\left(\frac{L}{Z_U}\right)^{\frac{11}{6}}\int_0^{Z_U} C_n^2(Z)\left[Z - \frac{Z^2}{Z_U}\right]^{\frac{5}{6}} dZ. \tag{4.2}
$$

As is conventional, h_a is taken to be Gamma-Gamma distributed [74]

$$
\Pr(h_a) = \frac{2(\alpha\beta)^{(\alpha+\beta)/2}}{\Gamma(\alpha)\Gamma(\beta)}(h_a)^{\frac{(\alpha+\beta)}{2}-1}K_{\alpha-\beta}(2\sqrt{\alpha\beta h_a})
$$

where $K_{\alpha-\beta}(\cdot)$ is the modified Bessel function of the second kind and α, β can be expressed with σ_{Bu} as [74, p.517].

$$
\begin{aligned}
1/\alpha &= e^{0.49\sigma_{Bu}^2/(1+0.56\sigma_{Bu}^{12/5})^{7/6}} - 1, \\
1/\beta &= e^{0.51\sigma_{Bu}^2/(1+0.69\sigma_{Bu}^{12/5})^{5/6}} - 1.
\end{aligned}
$$

The Gamma-Gamma scintillation model is applied both in Chap. 3 and Chap. 4.

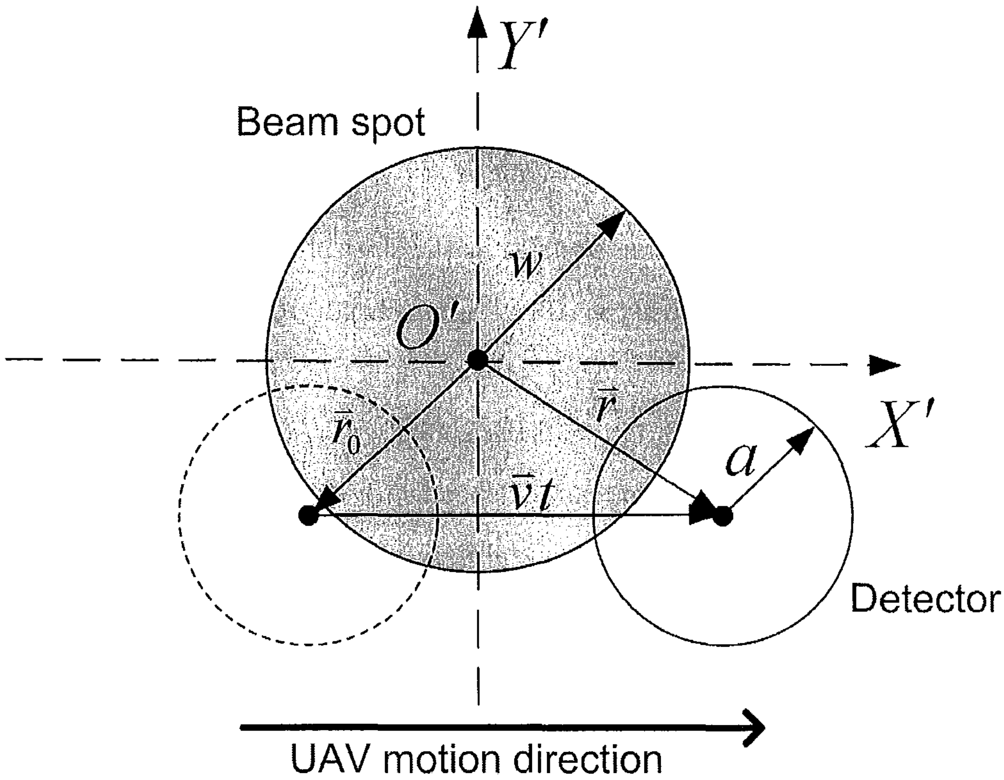

Figure 4.4: Misalignment between detector and beam spot

However, in this chapter, for the uplink channel, the parameters α and β are modified due to the σ_{Bu}^2 which takes atmospheric variation in different altitude Z into account.

4.1.2 Tracking Error

Since the beam width of the optical beam is much smaller than that of RF links, the tracking error is a major problem in FSO links. Figure 4.4 is a diagram of the beam spot in the transverse plane at the receiver in a given tracking interval T_{tr}. Define $\vec{r}(t)$ as the instantaneous distance between centers of the beam spot and the detector in a given tracking interval, i.e., $t \in [0, T_{tr})$ as

$$\vec{r}(t) = \vec{r}_0 + \vec{v}t \tag{4.3}$$

where $\vec{r}_0$ is the initial beam position at the start of the tracking interval (i.e., $t = 0$) and $\vec{v}$ is a constant velocity vector with magnitude 100 m/s.

At the start of each tracking interval, $\vec{r}_0$ is the random initial beam position as determined by the GPS data and the gimbal error. The initial misalignments in X' and Y' are modelled as identical, independent zero-mean Gaussian distributions with variance σ_{tr}^2. Based on experimental data of gimbal and GPS errors, $\sigma_{tr} = 3.3$ m with 99% confidence level [12]. Thus, $\vec{r}_0$ is modelled as being chosen randomly and independently at the start of each tracking interval whereas the variation of $\vec{r}$ within each tracking is known given $\vec{r}_0$.

Following [30], the intensity at the receiver due to misalignment can be estimated based on the instantaneous $\vec{r}$ in (4.3). This model for misalignment is developed for horizontal FSO links in previous work [30]. However, for the general consideration of Gaussian beam as introduced in Chap. 1, it is still suitable for uplinks. For the radius of detector a and laser beamwidth w, several parameters for tracking error h_{tr} are defined as below,

$$\begin{cases} q = \sqrt{\frac{\pi}{2}} \cdot \left(\frac{a}{w}\right) \\ A_0 = [\mathrm{erf}(q)]^2 \\ w_{\mathrm{eq}}^2 = w^2 \sqrt{\pi}\,\mathrm{erf}(q)/2qe^{-q^2} \end{cases}.$$

where w_{eq} is the equivalent beam width. The attenuation due to tracking error is [30],

$$h_{tr}(\vec{r}) \approx A_0 e^{-2\|\vec{r}\|^2/w_{\text{eq}}^2}. \tag{4.4}$$

It is important to note that the impact of h_{tr} is often a limiting factor in the design of such mobile FSO systems. The attenuation h_{tr} varies widely, even in a given T_{tr}, as the detector moves across the beam spot and often dominates over atmospheric scintillation. Statistical parameters of h_{tr} can be acquired from simulation in a given channel. Define $\langle h_{tr} \rangle$, σ_{htr} as the expectation and standard deviation of h_{tr} respectively, then the intensity of the fluctuation of h_{tr} is defined as ζ,

$$\zeta = \frac{\sigma_{htr}}{\langle h_{tr} \rangle}. \tag{4.5}$$

Different fluctuation intensities ζ exist according to different channel parameters, especially the beam divergence angle ϕ. If ϕ is small, high channel gain only exists when laser beam is in the FOV of receiver, otherwise channel gain is near zero. In contrast, if ϕ is big, laser beam stays in the FOV of receiver most of the time, but the average channel gain is low. This phenomenon is quantified with the comparison of $\phi = 1$, 2.5 and 4 mrad in Sec. 4.2.

4.1.3 Channel Model

The ground-to-UAV FSO channel considered in this work is modelled as a packet transmission system, and is shown in Fig. 4.5. A message is divided into k packets each of size 1 kbit. A sequence of Raptor coded outputs are generated from these message packets, as discussed in Chap. 2. A 32-bit CRC from the IEEE 802.3 standard [84] is added to each packet before transmission on the channel defined in (1.1) and (4.1). At

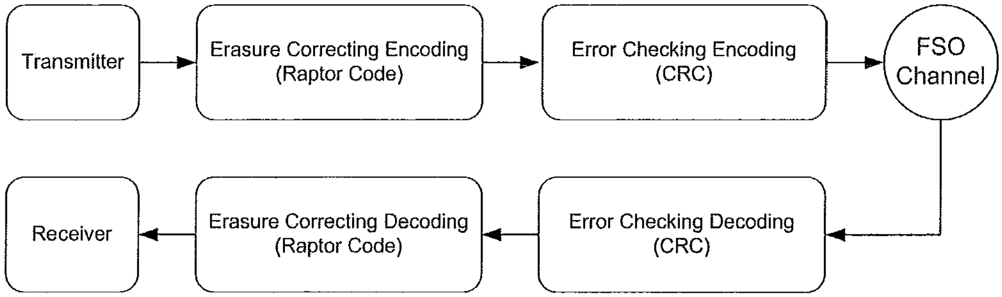

Figure 4.5: Packet-level channel model of ground-to-UAV FSO channel

the receiver, any corrupted packets are dropped and not used in the Raptor decoder. Since the probability of undetectable error for this CRC is $< 10^{-9}$, when bit error probability < 0.5 [84], the undetected packet errors at the receiver is ignored. Finally, the entire message is decoded when sufficient packets are received. In addition, it is assumed that the transmitter continues to send packets for a given message until it receives a 1-bit feedback from the receiver to move to the next message.

4.2 Simulation Results on FSO Channel

In this section, the Raptor codes of Chap. 2 are applied on the mobile FSO channel of Sec. 4.1.3. The channel state is randomly selected according to h_a and h_{tr} and Gaussian noise is added to each packet. The received packets that fail in the CRC check are discarded. As in Sec. 4.1.3, it is assumed that a one bit feedback is available to the transmitter to proceed to the next k-packet message. Link parameters are chosen as Tbl. 4.1

Conventional fixed-rate channel coding is not suitable for this channel because of the severe slow fading. The performance of the system with Raptor codes is compared to uncoded automatic repeat-request (ARQ) algorithm. Notice that ARQ

Table 4.1: Parameters of the ground-to-UAV FSO link for simulation

Parameter	Symbol	Value
Communication distance	L	$\sqrt{3}$ km
UAV altitude	Z_U	1 km
UAV speed	$\lvert\vec{v}\rvert$	100 m/s (360 km/h)
Tracking interval	T_{tr}	50 ms
Wavelength	λ	1550 nm
Transmission rate		1 Gbps
Transmitted power	P	$10 - 300$ mW ($10 - 25$ dBm)
Receiver responsivity	R	0.5 A/W
Variance of noise	σ_n	10^{-7} A
Laser divergence angle	ϕ	1, 2.5 mrad
Receiver diameter	$2a$	20 cm
Scattering coefficient	η	0.673 km^{-1} (2.92 dB/km)
Wind speed	s	30 m/s
Nominal ground turbulence	A	1.7×10^{-13} m$^{-2/3}$

requires that the transmitter must wait for feedback from the receiver for every packet. For a fair comparison, the total delay of packet propagation and feedback signal is considered. It is assumed that the 1-bit feedback for ARQ is perfect. Thus, the total delay is $2L/C = 11.5$ μs, where C is the speed of light. Note that this delay is much larger than the packet transmission duration 1 μs and severely limits rates using ARQ. The average data rates when using an OOK, 1 Gbps transmitter are simulated. The average transmit power, P, is varied from $10 - 300$ mW and the receiver noise standard deviation $\sigma_n = 10^{-7}$ A from [30]. The UAV speed is set to 100 m/s, and GPS updates happen every 50 ms for a total simulation duration of 100 s [12]. Other channel parameters are selected as mentioned in Sec. 3.1.

The Raptor code performance is simulated under two different beam divergence angle $\phi = 1$, 2.5 and 4 mrad respectively. With the definition of fluctuation intensity ζ in (4.5), the simulation result of tracking error is presented in Tbl. 4.2.

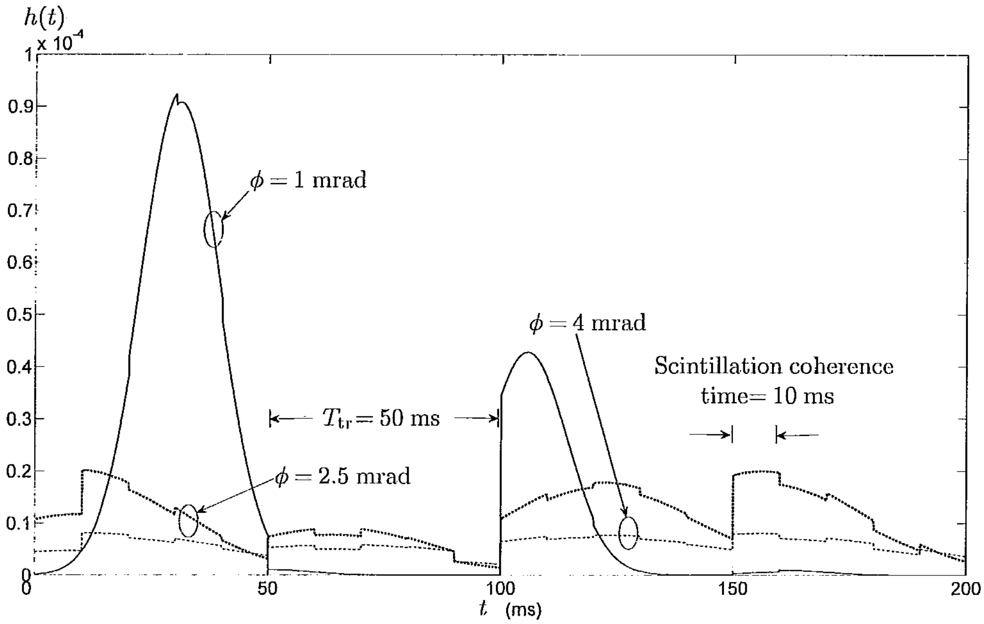

Figure 4.6: Slow fading $h(t)$ of the mobile FSO link with ϕ = 1, 2.5 and 4 mrad including h_l, h_a and h_{tr}

Table 4.2: Fluctuation intensity, ζ, and average tracking loss, $\langle h_{tr} \rangle$, for different ϕ

ϕ mrad	ζ	$\langle h_{tr} \rangle$
1	1.74	4.2×10^{-4}
2.5	0.45	2.9×10^{-4}
4	0.18	1.6×10^{-4}

The difference of ϕ causes significant difference of tracking error, as presented in Fig. 4.6 and Tbl. 4.2. For $\phi = 1$ mrad, the fluctuation is more severe than $\phi = 2.5$ mrad, but $\langle h_{tr} \rangle$ is greater. Data rates of the short-length Raptor codes ($k = 16-1024$) under these two ϕ are presented in Fig. 4.7 and 4.8 respectively. The packet erasure probability of the mobile FSO link is affected by both ϕ and transmitted power P. When $P < 13$ dBm, the data rate of $\phi = 1$ mrad is higher. However, when $P > 13$ dBm, the data rate of $\phi = 1$ mrad increases less than that of $\phi = 2.5$ mrad. However, when $\phi = 4$ mrad, since the $\langle h_{tr} \rangle$ is much lower than that of $\phi = 2.5$ mrad, the average data rate is lower. If ϕ increases to infinity, $\langle h_{tr} \rangle$ drops near zero.

Raptor codes are compared to the the capacity of the equivalent packet erasure channel and ARQ in Fig. 4.7, 4.8 and 4.9. The average data rate increases with P leaving a small gap to the erasure capacity. With increasing k, the average data rate also increases. It is obvious that the incremental performance improvement from $k = 512$ to 1024 is much smaller than that from $k = 16$ to 32. So, it is suggested that a practical choice is $k = 64$ which provides and average rate of 650 Mbps for $P = 20$ dBm with $\phi = 2.5$ mrad. Also from Chap. 2, in this case, only $d_{\text{avg}} = 4.14$ average operations per packet is needed and the hardware Raptor decoder can work at 714 Mbps at $k = 64$. It is a significant advantage to save the system cost on the UAV platform which is sensitive of weight and power consumption.

Notice that the maximum rate using ARQ is significantly smaller than the Raptor coded system. The short-length Raptor codes designed here improve the data rate from 70 Mbps to 650 Mbps with $\phi = 2.5$ mrad. In addition, the hardware Raptor encoder and decoder implemented in Chap. 2 are also suitable for the communication on UAVs. The rate improvement of short-length Raptor codes over ARQ requires a

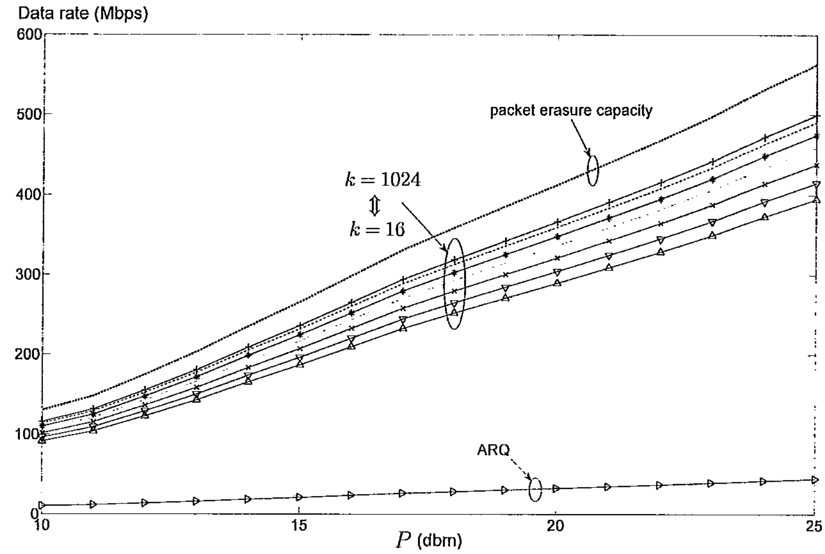

Figure 4.7: Average data rate versus transmitted power on mobile FSO channel when $\phi = 1$ mrad

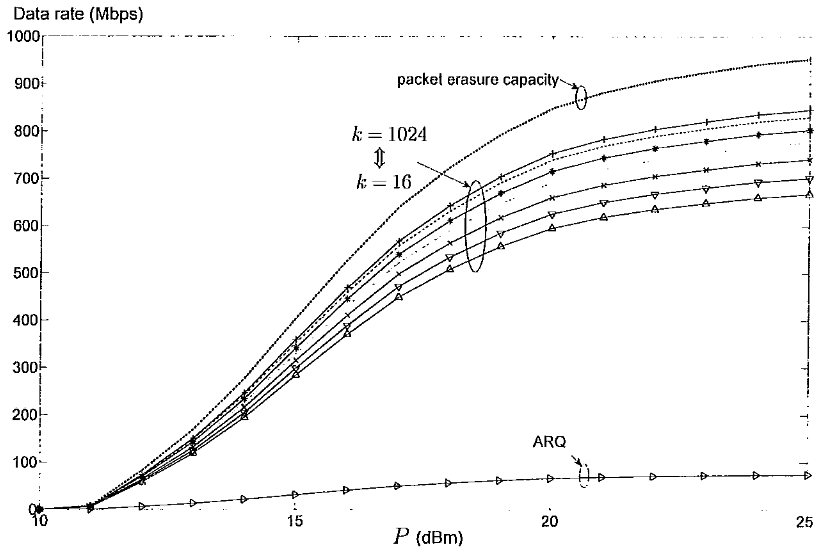

Figure 4.8: Average data rate versus transmitted power on mobile FSO channel when $\phi = 2.5$ mrad

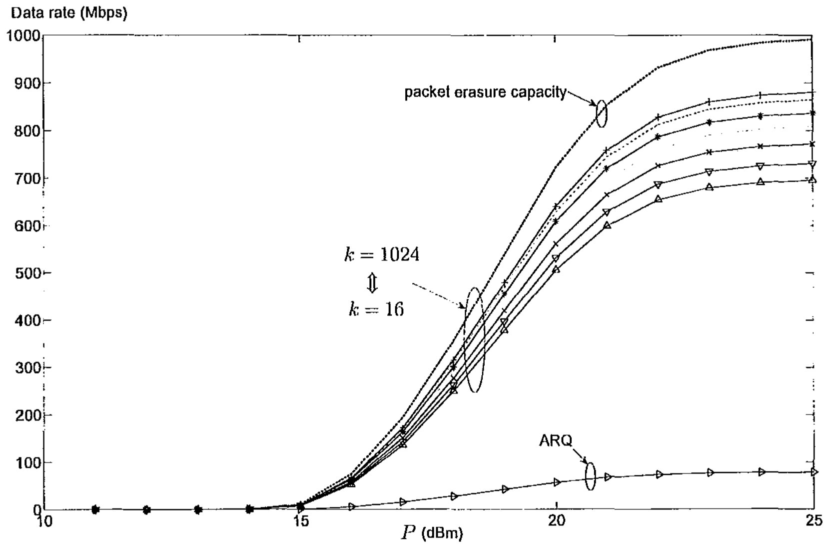

Figure 4.9: Average data rate versus transmitted power on mobile FSO channel when $\phi = 4$ mrad

small hardware cost and storage at both encoder and decoder.

4.3 Conclusions

In this work, short-length Raptor codes are applied for a ground-to-UAV mobile FSO channel. These codes are independent of channel misalignment caused by tracking error and atmosphere scintillation. Since the designed codes are independent of the channel state and have low complexity they are appropriate for a host of mobile FSO applications. Although the misalignment is large, where average tracking loss $\langle h_{tr} \rangle = 2.9 \times 10^{-4}$ for $\phi = 2.5$ mrad, for code length $k = 64$, the Raptor-coded mobile FSO channel offers average rates of 650 Mbps using a 1 Gbps transmitter and 20 dBm transmit power. The technique of FSO links and short-length Raptor codes can be also applied to ground-to-HAP channel as described in Chap. 1.

Chapter 5

Conclusion

5.1 Main Results of the Thesis

FSO links offer high data rate at Gbps level and simpler architecture than RF links. However, the slow fading due to atmospheric scintillation and tracking error of FSO links affect the data rate. Current fixed-length coding schemes are unable to overcome this slow fading because of the fading interval at 10's ms and high transmission rate at Gbps. In this work, Raptor codes which are a linear random codes are considered to adapt to channel capacity. Also, for mobile FSO links where channel state varies widely, Raptor codes can adapt to channel conditions with little feedback.

A set of short-length Raptor codes ($k = 16 - 1024$) are designed and implemented. These codes combine the advantages of high rate and low decoding complexity. The overhead of these codes are $42 - 12\%$ and the average decoding operation is $2.5 - 6.3$. These short-length Raptor codes can be easily implemented in PC with software. Also, it can be implemented in hardware FPGA with small scale and low power consumption. A practical Raptor encoder and decoder are implemented in FPGA and shown to support a 714 Mbps data rate with a low 97 mW power consumption and 26360 gate circuit scale. They are suitable for high-speed transmission at Gbps level for a wide range of applications.

Two applications of short-length Raptor codes are presented. Firstly, in Chap. 3, the short-length Raptor codes are applied in hybrid FSO/RF links to achieve high data rate to utilize the capacities of the FSO and RF links simultaneously. The performance of these Raptor codes is simulated in a realistic channel model based on climate data for three Canadian cities. For a 1 Gbps FSO link combined with a 96 Mbps WiMAX RF link, the soft-switching system achieves an average rate of over 472 Mbps using the implemented Raptor code while hard-switching techniques achieved only 112 Mbps on average in these three cities.

Secondly, in Chap. 4, these Raptor codes are applied in mobile FSO links for UAV to overcome the severe jitter. Under practical link parameters, the erasure correction performance of these Raptor codes is simulated. With a 1 Gbps transmitter, the designed Raptor code with $k = 64$ message packets offers 560 Mbps data rate when transmitting power is 20 dBm. In contrast, a traditional automatic repeat-request (ARQ) algorithm technique on the same FSO jitter channel achieves a rate of 60 Mbps.

5.2 Future Work

The hardware Raptor encoder and decoder can be implemented in ASIC with a much higher clock frequency operating at the GHz level. With this clock frequency, the encoding and decoding rate can easily reach several Gbps which is a significant improvement from the implementation in FPGA. Also, the architecture of the encoder and decoder can be simplified with a smaller random number generator for the degree and

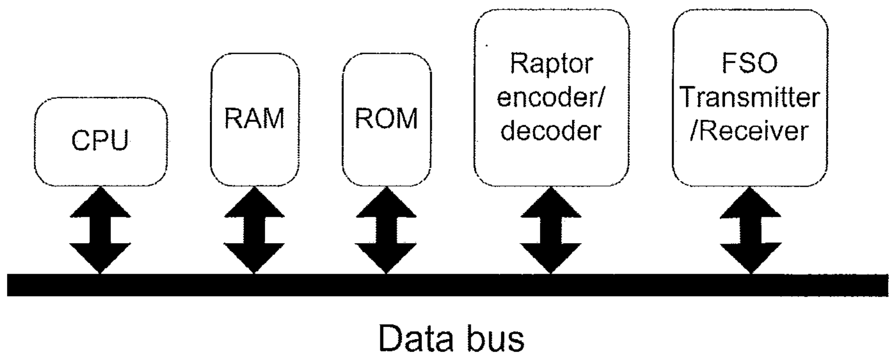

Figure 5.1: Future ASIC Raptor encoder/decoder applied in system level

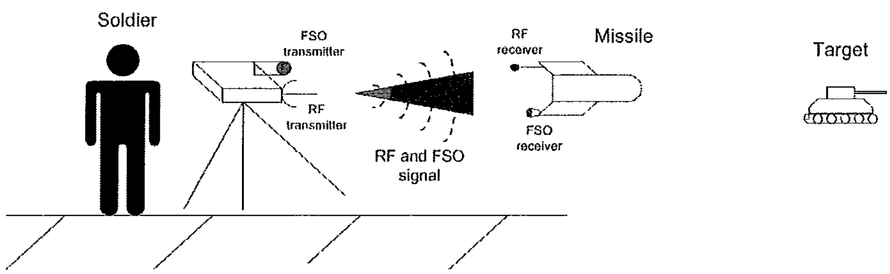

Figure 5.2: A future military hybrid FSO/RF link with Raptor codes

connection information between packets. Future Raptor coding systems can be implemented in a real system which contains CPU, RAM, Raptor encoder/decoder, buffer and FSO transmitter/receiver as presented in Fig. 5.1. The Raptor encoder/decoder is easily added to the data bus and only to act as a co-processor for the CPU. The convenience of the hardware Raptor coding makes it attractive for many high-speed communication applications.

The idea of hybrid FSO/RF links with Raptor codes presented in Chap. 3 can be implemented in an experiment setup with an FSO link and a WiMAX or WiFi RF link in the future. The design of this combined links can be optimized to minimize the weight, size and power consumption. This hybrid application is a competitive for the future point-to-point wireless communication. For mobile applications, it is possible

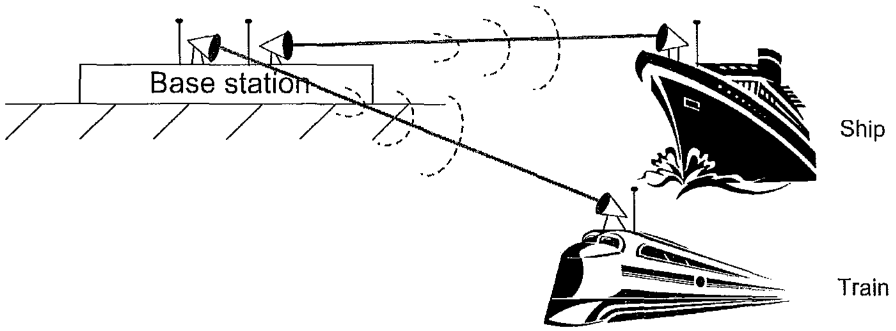

Figure 5.3: Future shore-to-ship and station-to-train hybrid FSO/RF links

to design an integrated FSO/RF transmitter and receiver. Due to its small diameter, the laser diode of FSO transmitter can be placed on the RF transmitter antenna. Also, the FSO receiver optics can be integrated with the RF receiver antenna. This integration saves size of the hybrid link significantly and it is useful even for portable platforms or small military platforms such as missiles. A possible military use of this hybrid link is for a short-range missile system presented in Fig. 5.2. A soldier launches a missile toward the target and send target motion information through the hybrid link. The missile adjusts its attitude according to the information. Since the carrier frequency of FSO and RF link is far different, and the both of them are LOS links, the hybrid link has high reliability avoiding jamming.

Also, for civil applications, presented in Fig. 5.3, this integrated terminals of hybrid links can be employed on train and ship as shore-to-ship and station-to-train high-speed links. The applications of this hybrid link can satisfy the reliability requirement of many future wireless communication applications.

Bibliography

[1] E. Kube, "Information Transmission by Light Beams through the Atmosphere," *J. Nachrichtentechnik*, vol. 6, pp. 201–207, Jun. 1968.

[2] "FSO History and Technology," `http://www.laseroptronics.com/index.cfm/id/57-66.htm`. Laseroptronics, [online], last accessed: Mar. 30, 2009.

[3] "GeoDesy FSO Giga Super," `http://www.geodesy-fso.com/user_files/download/geodesy_fso_giga_super.pdf`. GeoDesy Kft, [online], last accessed: Mar. 30, 2009.

[4] "Airlinx Canobeam DT-100 Series Data Sheet," `http://www.airlinx.com/files/AIRLINXCanobeamDT-100SeriesDataSheet0606.pdf`. AIRLINX Communications Inc, [online], last accessed: Mar. 30, 2009.

[5] "SONAbeam Datasheets," `http://www.fsona.com/prod/SONAbeam-Datasheets.pdf`. fSONA, [online], last accessed: Mar. 30, 2009.

[6] "Solectek FSO-100E Optical Wireless PTP Links," `http://www.solectek.com/files/pdf/datasheets/FSO-100E.pdf`. [online], last accessed: Mar. 30, 2009.

[7] M. C. Jeong, J. S. Lee, S. Y. Kim, S. W. Namgung, J. H. Lee, M. Y. Cho, S. W. Huh, and J. S. Lee, "8×10 Gb/s Terrestrial Optical Free Space Transmission

over 3.4 km Using an Optical Repeater," *Proc. IEEE Opt. Fiber Commun. Conf. Exhib.*, pp. 405–407, Mar. 2002.

[8] E. Leitgeb, M. Gebhart, and U. Birnbacher, "Optical Networks, Last Mile Access and Applications," *J. Opt. Fiber Commun. Res.*, vol. 2, no. 1, pp. 56–85, Mar. 2005.

[9] "Gigabit-speed FSO Network Serves Istanbul's Business District," `http://lw.pennnet.com/Articles/Article_Display.cfm?Section=Articles&ARTICLE_ID=208105&VERSION_NUM=1`. [online], last accessed: Mar. 30, 2009.

[10] "Free Space Optics (FSO) Global Market Forecast," `http://www.dri.co.jp/auto/report/elecast/ec30600702.htm`. [online], last accessed: Mar. 30, 2009.

[11] J. Horwath, N. Perlot, M. Knapek, and F. Moll, "Experimental Verification of Optical Backhaul Links for High Altitude Platform Networks: Atmospheric Turbulence and Downlink Availability," *Int. J. Satellite Commun. Networking*, vol. 25, pp. 501–528, 2007.

[12] T. I. King, H. H. Refai, J. J. S. Jr., and Y. Lee, "Control System Analysis for Ground/Air-To-Air Laser Communications Using Simulation," *Proc. IEEE 24th Digital Avionics Syst. Conf.*, pp. 1.C.3–1–1.C.3–7, 2005.

[13] A. Harris, J. J. S. Jr., and H. H. Refai, "Alignment and Tracking of a Free-Space Optical Communication Link to a UAV," *Proc. IEEE 24th Digital Avionics Syst. Conf.*, pp. 1.C.2–1–1.C.2–9, 2005.

[14] H. Henniger, D. Giggenbach, J. Horwath, and C. Rapp, "Evaluation of Optical Up- and Downlinks from High Altitude Platforms Using IM/DD," *Proc. SPIE*, vol. 5712, pp. 24–36, 2005.

[15] H. Manor and S. Arnon, "Performance of an Optical Wireless Communication System as a Function of Wavelength," *Appl. Opt.*, vol. 42, pp. 4285–4294, 2003.

[16] D. Giggenbach, J. Horwath, and B. Epple, "Optical Satellite Downlinks to Optical Ground Stations and High-Altitude Platforms," *Proc. IEEE IST Mobile & Wireless Commun. Summit*, pp. 1–4, 2007.

[17] "Unmanned Aerial Vehicles (UAVs)," `http://www.fas.org/irp/program/collect/uav.htm`. [online], last accessed: Mar. 30, 2009.

[18] "The Website for the Defence Industries-Air Force Unmanned Aerial Vehicles (UAV)," `http://www.airforce-technology.com/contractors/uav/`. [online], last accessed: Mar. 30, 2009.

[19] "Unmanned Airship Solutions for Integrated ISR and Communications Systems," `http://www.sanswiretao.com/Sanswire-UAV.pdf`. Sanswire Corporation, [online], last accessed: Mar. 30, 2009.

[20] T. C. Tozer and D. Grace, "High-Altitude Platforms for Wireless Communications," *IEE Electron. Commun. Eng. J.*, pp. 127–137, Jun. 2001.

[21] "The X-Station Product Datasheet," `http://www.stratxx.com/files/downloads/x-station_product_sheet.pdf`. StratXX Near Space Technology AG, [online], last accessed: Mar. 30, 2009.

[22] "High Altitude Platform Stations for Australia," `http://www.stratocomm.net/AustralianWhitePaper.pdf`. Sky Station and StratoComm Corporation, [online], last accessed: Mar. 30, 2009.

[23] D. Grace, J. Thornton, T. Konefal, C. Spillard, and T. C. Tozer, "Broadband Communications from High Altitude Platforms - the HeliNet Solution," *Proc. Wireless Personal Mobile Conf.*, Sep. 2001.

[24] B. Taha-Ahmed, M. Calvo-Ramon, and L. D. Haro-Ariet, "UMTS-HSDPA in High Altitude Platforms (HAPs) Communications," *Turkish J. Electr. Eng. Comput. Sci.*, vol. 15, no. 1, no. 1, pp. 105–112, 2007.

[25] D. J. T. Heatley, D. R. Wisely, I. Neild, and P. Cochrane, "Optical Wireless: The Story So Far," *IEEE Communn. Mag.*, vol. 36, no. 12, pp. 72–82, Dec. 1998.

[26] S. Hranilovic, *Wireless Optical Communications Systems.* Springer press, 2004.

[27] J. R. Barry, *Wireless Infrared Communications.* Kluwer Academic Publishers, 1994.

[28] J. M. Kahn and J. R. Barry, "Wireless Infrared Communications," *Proc. IEEE*, vol. 85, no. 2, pp. 263–298, Feb. 1997.

[29] X. Zhu and J. M. Kahn, "Free-Space Optical Communication through Atmospheric Turbulence Channels," *IEEE Trans. Commun.*, vol. 50, no. 8, pp. 1293–1300, Aug. 2002.

[30] A. A. Farid and S. Hranilovic, "Outage Capacity Optimization for Free-Space Optical Links With Pointing Errors," *IEEE J. Lightwave Tech.*, vol. 25, no. 7, pp. 1702–1710, Jul. 2007.

[31] E. Leitgeb, M. Gebhart, and P. Fasser, "Reliability of Free Space Laser Communications-Investigations at the TU Graz," *Proc. Annu. WCA Tech. Symp.*, pp. 579–586, Jan. 2002.

[32] D. Kedar and S. Arnon, "Urban Optical Wireless Communication Networks: The Main Challenges and Possible Solutions," *IEEE Commun. Mag.*, vol. 42, no. 5, pp. S2–S7, May 2004.

[33] S. Arnon, "Effects of Atmospheric Turbulence and Building Sway on Optical Wireless Communication Systems," *Opt. Lett.*, vol. 28, no. 2, pp. 129–131, Jan. 2003.

[34] D. Kedar and S. Arnon, "Optical wireless communication through fog in the presence of pointing errors," *Appl. Opt.*, vol. 42, no. 24, pp. 4946–4954, Aug. 2003.

[35] A. Shokrollahi, "Raptor codes," *IEEE Trans. Inform. Theory*, vol. 52, no. 6, pp. 2551–2567, Jun. 2006.

[36] R. Palanki and J. S. Yedidia, "Rateless Codes on Noisy Channels," *Proc. IEEE Int. Symp. Inform. Theory*, p. 38, 2004.

[37] "Universal Mobile Telecommunication Systems; Multimedia Broadcast/Multicast Service; Protocols and codecs," *ETSI 3GPP TS 26.346 version 6.3.0 Release 6*, Dec. 2005.

[38] M. Luby, "LT codes," *Proc. ACM Symp. Found. Comput. Sci.*, pp. 271–280, 2002.

[39] "DF Raptor Technology Datasheet," `http://www.digitalfountain.com/df-raptor-technology-datasheet.html`. Digital Fountain, [online], last accessed: Mar. 30, 2009.

[40] A. AbdulHussein, A. Oka, and L. Lampe, "Rateless Coding for Hybrid Free-Space Optical and Radio-Frequency Communication," *submitted to IEEE Trans. Wireless, under review.*

[41] I. I. Kim and E. J. Korevaar, "Availability of Free Space Optics (FSO) and Hybrid FSO/RF Systems," *Proc. SPIE*, pp. 84–95, Nov. 2001.

[42] E. Leitgeb, M. Gebhart, U. Birnbacher, W. Kogler, and P. Schrotter, "High Availability of Hybrid Wireless Networks," *Proc. SPIE*, pp. 238–249, Sep. 2004.

[43] "System Support Solutions," `http://www.systemsupportsolutions.com/models.htm`. [online], last accessed: Mar. 30, 2009.

[44] J. Derenick, C. Thorne, and J. Spletzer, "Hybrid Free-Space Optics/Radio Frequency (FSO/RF) Networks for Mobile Robot Teams," "Multi-Robot Systems: From Swarms to Intelligent Automata," A. C. Schultz and L. E. Parker (eds.), Springer, Mar. 2005.

[45] S. D. Milner and C. C. Davis, "Hybrid Free Space Optical/RF Networks for Tactical Operations," *Proc. IEEE Mil. Commun. Conf.*, pp. 409–415, 2004.

[46] A. Akbulut, H. G. Ilk, and F. Ari, "Design, Availability and Reliability Analysis on an Experimental Outdoor FSO/RF Communicaiton System," *Proc. IEEE Int. Conf. Transparent Opt. Networks*, pp. 403–406, 2005.

[47] S. Vangala and H. Pishro-Nik, "Optimal Hybrid RF-Wireless Optical Communication for Maximum Efficiency and Reliability," *Proc. IEEE Annu. Conf. Inform. Sci. Syst.*, pp. 684–689, 2007.

[48] V. Gadwal and S. Hammel, "Free-space Optical Communication Links in a Marine Environment," *Proc. SPIE*, vol. 6304, pp. 1–11, 2006.

[49] A. Biswas and S. Piazzolla, "Deep-Space Optical Communications Downlink Budget from Mars: System Parameters," 2003. Interplanetary Network Progress Report, Jet Propulsion Laboratory.

[50] C. Anderson, "Transformational Communitions rev.5,," `http://sunset.usc.edu/GSAW/gsaw2002/s8/canderson.pdf`, 2002. MILSATCOM Joint Program Office, [online], last accessed: Mar. 30, 2009.

[51] Z. W, H. Kumar, and A. Davari, "Performance Evaluation of OFDM Transmission in UAV Wireless Communication," *Proc. 37th Southeastern Symp. Syst. Avionics*, pp. 6–10, 2005.

[52] C. Chlestil, E. Leitgeb, N. Schmitt, S. S. Muhammad, K. Zettl, and W. Rehm, "Reliable Optical Wireless Links within UAV Swarms," *Proc. IEEE Int. Conf. Transparent Opt. Networks*, vol. 4, pp. 39–42, Jun. 2006.

[53] E. Leitgeb, K. Zettl, S. S. Muhammad, N. Schmitt, and W. Rehm, "Investigation in Free Space Optical Communication Links Between Unmanned Vehicles (UAVs)," *Proc. IEEE Int. Conf. Transparent Opt. Networks*, vol. 3, pp. 152–155, Jul. 2007.

[54] A. Harris, J. J. S. Jr., H. H. Refai, and P. G. LoPresti, "Atmospheric Turbulence Effects on a Wavelength Diversified Ground-To-UAV FSO Link," *Proc. SPIE*, vol. 6105, pp. 1–11, 2006.

[55] W. Zhang and S. Hranilovic, "Soft-Switching Hybrid FSO/RF Links Using Short-length Raptor Codes: Design and Implementation," *submitted to IEEE J. Select. Areas Commun., under review.*

[56] W. Zhang and S. Hranilovic, "Short-Length Raptor Codes for Mobile Free-Space Optical Channels," *IEEE Int. Conf. Commun.*, 2009.

[57] E. Hepsaydir, E. Witvoet, N. Binucci, and S. Jadhav, "Enhanced MBMS in UMTS Networks and Raptor Codes," *Proc. Annu. IEEE Int. Symp. Personal, Indoor and Mobile Radio Commun.*, pp. 1–5, Sep. 2007.

[58] N. Thomos and P. Frossard, "Raptor Network Video Coding," *Proc. the 1st ACM Int. Workshop on Mobile Video*, pp. 19–24, Sep. 2007.

[59] R. Schiphorst, X. Shao, and K. Slump, "Reliable Download Delivery in a Terrestrial DAB Network," *Proc. 29th Symp. Inform. Theory in the Benelux*, pp. 105–111, May 2008.

[60] F. Uyeda, H. Xia, and A. A. Chien, "Evaluation of a high performance erasure code implemention," Sep. 2004. Report prepared for Computer Science and Engineering Department, University of California, San Diego.

[61] "Virtex-II Pro and Virtex-II Pro X Platform FPGAs: Complete Data Sheet DS083 (v4.7)," `www.xilinx.com/support/documentation/data_sheets/ds083.pdf`. Xilinx, [online], last accessed: Mar. 30, 2009.

[62] "ISE 9.1 In-Depth Tutorial," `http://download.xilinx.com/direct/ise9_tutorials/ise9tut.pdf`. Xilinx, [online], last accessed: Mar. 30, 2009.

[63] "XPE Web Power Tools," `http://www.origin.xilinx.com/cgi-bin/power-tool/power_virtex2p`. Xilinx, [online], last accessed: Mar. 30, 2009.

[64] I. I. Kim, B. McArthur, and E. Korevaar, "Comparison of Laser Beam Propagation at 785 nm and 1550nm in Fog and Haze for Optical Wireless Communications," *Proc. SPIE*, vol. 4214, pp. 26–37, Feb. 2001.

[65] M. Jeganathan and P. Ionov, "Multi-Gigabits-per-second Optical Wireless Communications," `http://www.freespaceoptic.com/WhitePapers/Jeganathan(OpticalCrossing).pdf`. [online], last accessed: Mar. 30, 2009.

[66] E. J. McCartney, *Optics of the Atmosphere.* Wiley press, 1976.

[67] D. Atlas, "Shorter Contribution Optical Extinction by Rainfall," *J. Meterol.*, vol. 10, pp. 486–488, 1953.

[68] R. O. Gumprecht and C. M. Sliepcevich, "Scattering of Light by Large Spherical Particles," *J. Phys. Chem.*, vol. 57, pp. 90–97, 1953.

[69] W. E. Middleton, *Vision Through the Atmosphere.* University of Toronto Press, 1952.

[70] H. W. O'Brien, "Visibility and Light Attenuation in Falling Snow," *J. Appl. Meteorol.*, pp. 671–683, 1970.

[71] A. C. Best, "The Size Distribution of Raindrops," *Quart. J. R. Meteor. Soc.*, vol. 76, pp. 16–36, 1950.

[72] J. S. Marshall and W. M. Palmer, "The Distribution of Raindrops with Size," *J. Meteor.*, vol. 5, pp. 165–166, 1948.

[73] K. Itoo, N. Yano, and K. Hama, "Size Distribution, Crystal Form and Falling Velocity of Snow-Flake," *J. Meteor. Soc. Japan*, vol. 31, pp. 25–37, 1953.

[74] L. C. Andrews and R. L. Phillips, *Laser Beam Propagation through Random Media.* SPIE press, second ed., 2005.

[75] A. A. Farid and S. Hranilovic, "Optimization of Beam Width, Bit Error Rate and Availability for Free-Space Optical Links," *Proc. IEEE Int. Symp. Commun. Syst. Network Digital Signal Processing*, pp. 92–96, 2008.

[76] E. Korevaar, I. I. Kim, and B. McArthur, "Atmospheric Propagation Characteristics of Highest Importance to Commercial Free Space Optics," *Proc. SPIE*, vol. 4976, pp. 1–12, Apr. 2003.

[77] "Tsunami^{tm} MP.11 Model 5054 Technical Specifications," `http://www.proxim.com/products/bwa/multipoint/mp11`. [online], last accessed: Mar. 30, 2009.

[78] "IEEE Standard for Local and Metropolitan Area Networks Part 16: Air Interface for Fixed Broadband Wireless Access Systems," 2004. IEEE Std 802.16^{TM}-2004.

[79] R. L. Olsen, D. V. Rogers, and D. B. Hodge, "The aR^b Relation in the Calculation of Rain Attenuation," *IEEE Trans. Antennas Propag.*, vol. AP-26, no. 2, pp. 318–329, Mar. 1978.

[80] D. K. Cheng, *Field And Wave Electromagnetics.* Addison-Wesley Publishing Company, 1983.

[81] "WiMAX Antenna," http://www.WiMAX-industry.com/ar/10u.htm. [online], last accessed: Mar. 30, 2009.

[82] "GigaBeam 5.8 Series PtP datasheet," http://www.gigabeam.com/PDFs/GigaBeam5.8PtPdatasheet.pdf. [online], last accessed: Mar. 30, 2009.

[83] "Telsima's Sub-GHz WiMAX(TM) System Demonstrates a 50km (30mile) High Capacity Broadband Internet Connection at 450MHz," http://www.telsima.com/pic/pdf/download/Demo_Brief-50km.pdf. [online], last accessed: Mar. 30, 2009.

[84] T. Fujiwara, T. Kasami, and S. Lin, "Error Detecting Capabilities of the Shortened Hamming Codes Adopted for Error Detection in IEEE Standard 802.3," *IEEE Trans. Commun.*, no. 9, pp. 986–989, Sep. 1989.

[85] S. A. Ahson and M. Ilyas, *WiMAX Handbook.* CRC Press, 2007.

[86] "Canada's National Climate Archive," http://www.climate.weatheroffice.ec.gc.ca/. [online], last accessed: Mar. 30, 2009.

[87] "Fog, Canadian Encyclopedia," http://www.thecanadianencyclopedia.com. [online], last accessed: Mar. 30, 2009.

[88] "MQ-1 Predator Unmanned Aircraft System," http://www.af.mil/factsheets/factsheet.asp?fsID=122. [online], last accessed: Mar. 30, 2009.

[89] "RQ-4A/B Global Hawk High-Altitude, Long-Endurance, Unmanned Reconnaissance Aircraft," http://www.airforce-technology.com/projects/global/specs.html. [online], last accessed: Mar. 30, 2009.

[90] "Global Aircraft," http://www.globalaircraft.org. [online], last accessed: Mar. 30, 2009.

[91] G. M. Gofbauer and L. T. Kulikov, "Tu-143 "Reis"," http://ram-home.com/ram-old/tu-143.html. [online], last accessed: Mar. 30, 2009.

[92] "Automatic UAV Tracking System," http://www.covert-systems.com/uav/kss-ats-2-uav.html. [online], last accessed: Mar. 30, 2009.

[93] "UAV Tracking Systems," http://www.colmek.com/uav-tracking.html. [online], last accessed: Mar. 30, 2009.

[94] S. Rathinam, P. Almeida, Z. W. Kim, S. Jackson, A. Tinka, W. Grossman, and R. Sengupta, "Autonomous Searching and Tracking of a River Using an UAV," *Proc. American Control Conf.*, pp. 359–364, Jul. 2007.

[95] "Canadian Spatial Reference System GPS Accuracy Levels," http://www.geod.nrcan.gc.ca/edu/geod/gps/gps13_e.php. [online], last accessed: Mar. 30, 2009.

[96] "GPS6185HR PC/104 Peripheral Module GPS Satellite Receiver for Automotive and Mobile Systems," http://www.rtd.com/PC104/UM/GPS/GPS6185.htm. [online], last accessed: Mar. 30, 2009.

[97] "MS860 Rugged Dual-Antenna GPS Receiver for Precise Heading and Position," http://www.hydronav.com/images/Hydrographic/pdf/MS_860_8_00.pdf. [online], last accessed: Mar. 30, 2009.

[98] "Copernicus II GPS Receiver," http://www.contradata.it/download/Copernicus_II.pdf. Trimble, [online], last accessed: Mar. 30, 2009.